UNIVERSITY OF OKLAHOMA

GRADUATE COLLEGE

---

# Modeling of Inflation Rates and Mechanical Creation of Reflective Sphere to Harness Solar Radiation Pressure for Medium Earth Orbit Satellites

---

A THESIS
SUBMITTED TO THE GRADUATE FACULTY

*in partial fulfillment of the requirements for the*
*Degree of*

MASTER OF SCIENCE

*By:* Tara J. ELDRIDGE

Norman, Oklahoma

2025

**Modeling of Inflation Rates and Mechanical Creation of Reflective Sphere to Harness Solar Radiation Pressure for Medium Earth Orbit Satellites**

A THESIS APPROVED FOR THE
SCHOOL OF AEROSPACE AND MECHANICAL ENGINEERING

BY THE COMMITTEE CONSISTING OF

DR. DIOGO MERGUIZO SANCHEZ, CHAIR

DR. PRAKASH VEDULA

DR. JINGYAO DAI

UNIVERSITY OF OKLAHOMA

# *Abstract*

Department of Aerospace and Mechanical Engineering

Master of Science in Mechanical Engineering

**Modeling of Inflation Rates and Mechanical Creation of Reflective Sphere to Harness Solar Radiation Pressure for Medium Earth Orbit Satellites**

by Tara J. ELDRIDGE

This study proposes a dynamic model for the trajectory of a non-functional satellite with an inflatable spherical solar sail that acts as a de-orbiting device by harnessing Solar Radiation Pressure (SRP) and varying area-to-mass ratios. The model mimics real-world behaviors by using equations of motion that feature natural perturbations and SRP calculations using the cannonball model and shadow function. The time needed for the proposed balloon to push medium Earth orbit space debris back into the atmosphere is calculated for various binary and linear inflation methods. The results indicate that for satellites in near-circular orbits with an initial semi-major axis of 22,000 km, the solar sail can be deployed to push them into atmospheric re-entry within about 34.96 or 50.14 years for initial orbital inclinations of 0.001 or 56.06 degrees, respectively. For a GPS satellite with a semi-major axis of 26,560 km and inclination of 55 degrees, de-orbiting occurs within 61.3602 years. There is a potential for the improvement of these times by using a larger balloon or more reflective material. Alternative materials and compressor specifications are explored, though future advancements in these technologies are required to prove the feasibility of a mechanical model.

# Acknowledgements

First and foremost, I would like to extend my heartfelt gratitude to Professor Diogo Merguizo Sanchez for granting me the opportunity to pursue this research. His mentorship, patience, and contagious passion for astrodynamics have been instrumental in shaping my professional and personal growth. I would also like to acknowledge his hard work in creating the baseline orbital simulator within which this model has been coded.

I am immensely grateful to the faculty and staff in the Department of Aerospace and Mechanical Engineering at the University of Oklahoma for providing me with the encouragement and necessary resources that made this work possible. My sincere thanks also go to my committee members, Professor Prakash Vedula and Professor Jingyao Dai, for their thoughtful feedback and constructive suggestions that have greatly strengthened the quality of my research.

To my friends, roommates, and colleagues, thank you for your constant encouragement, thought-provoking discussions, and endless humor throughout this endeavor. I would also like to thank my high school Physics teacher, Mr. Gerald Davenport, for sparking my curiosity about space and setting me on the path of scientific exploration.

Lastly, I would like to express my appreciation for my family, without whom my academic pursuits would not have been possible. Thank you for providing me with unwavering support, picking up my late-night calls, and always pushing me to do my best.

Thank you all for being a part of this journey.

# Contents

# List of Figures

# List of Abbreviations

| | |
|---|---|
| **EOM** | Equation of Motion |
| **GEO** | Geostationary Orbit |
| **GLONASS** | Global'naya Navigatsionnaya Sputnikovaya Sis-tema |
| **GNSS** | Global Navigation Satellite Systems |
| **GPS** | Global Positioning System |
| **IADC** | Inter-Agency Space Debris Coordination Committee |
| **IKAROS** | Interplanetary Kite-craft Accelerated by Radiation Of the Sun |
| **JPL** | Jet Propulsion Laboratory |
| **LEO** | Low Earth Orbit |
| **MEO** | Medium Earth Orbit |
| **NASA** | National Aeronautics and Space Administration |
| **ODE** | Ordinary Differential Equations |
| **SRP** | Solar Radiation Pressure |
| **UN** | United Nations |

# Physical Constants

| | |
|---|---|
| Earth Standard Gravitational Parameter | $\mu_{\oplus} = 3.986\,013\,50 \times 10^{5}\,\mathrm{km}^3/\mathrm{s}^2$ |
| Moon Standard Gravitational Parameter | $\mu_{☾} = 4.902\,811\,40 \times 10^{3}\,\mathrm{km}^3/\mathrm{s}^2$ |
| Sun Standard Gravitational Parameter | $\mu_{\odot} = 1.327\,113\,84 \times 10^{11}\,\mathrm{km}^3/\mathrm{s}^2$ |
| Earth Volumetric Mean Radius | $R_{\oplus} = 6378.1366\,\mathrm{km}$ |
| Sun Volumetric Mean Radius | $R_{\odot} = 695\,700\,\mathrm{km}$ |
| Solar Constant | $S = 1367\,\mathrm{W}/\mathrm{m}^2$ |
| Radiation Intensity at Photosphere | $S_0 = 63.15 \times 10^{6}\,\mathrm{W}/\mathrm{m}^2$ |
| Solar Radiation Pressure | $P_{SR} = 4.563\,16 \times 10^{-6}\,\mathrm{N}/\mathrm{m}^2$ |
| Speed of Light | $c = 2.997\,924\,58 \times 10^{8}\,\mathrm{m}/\mathrm{s}$ |
| Second Zonal Harmonic of Earth | $J_2 = 1.082\,635\,9 \times 10^{-3}$ |
| Pi | $\pi = 3.141\,59$ |

# List of Symbols

| | | |
|---|---|---|
| $\oplus$ | Earth | non-dimensional |
| $☾$ | Moon | non-dimensional |
| $\odot$ | Sun | non-dimensional |
| | | |
| $\mathbf{r}$ | position | km |
| $\mathbf{v}$ | velocity | km/s |
| $\mathbf{a}$ | acceleration | km$^2$/s |
| $\theta$ | angle | rad |
| | | |
| $x$ | distance | km |
| $y$ | distance | km |
| $d$ | distance | km |
| | | |
| $R$ | radius | km |
| $A$ | area | m$^2$ |
| $m$ | mass | kg |
| $AM$ | area-to-mass ratio | m$^2$/kg |
| | | |
| $T$ | period | s |
| $t$ | time | s |
| $N$ | period fraction denominator | non-dimensional |
| $n$ | number of steps | non-dimensional |
| $h$ | step indicator number | non-dimensional |
| | | |
| $a$ | semi-major axis | km |
| $\omega$ | argument of the perigee | deg |
| $\dot{\Omega}$ | longitude of the ascending node | deg |
| | | |
| $C_R$ | radiation pressure coefficient | non-dimensional |
| $\varepsilon$ | reflectivity | non-dimensional |

| | | |
|---|---|---|
| $\dot{m}$ | mass flow rate | kg/s |
| $n_{mol}$ | number of moles | mol |
| $M_{mol}$ | molar mass | kg/mol |
| $P$ | pressure | Pa |
| $V$ | volume | $m^3$ |
| $\tau$ | temperature | K |

# Chapter 1

# Introduction

## 1.1 Space Debris

When the Soviet Union first launched the Sputnik I satellite into orbit in October 1957, the space around the Earth was entirely untouched by artificial devices. However, in the decades since, it has become increasingly challenging for missions launching new spacecraft into orbit to avoid crashing into existing satellite fleets, spent rocket stages, and other devices. While functional satellites could be directed out of a collision path in the worst-case scenario, the same cannot be said for space debris, which are defined by the Inter-Agency Space Debris Coordination Committee (IADC) as "all human made objects including fragments and elements thereof, in Earth orbit or re-entering the atmosphere, that are non-functional"[1]. These non-steerable objects are left to the whims of nature, slowly being pushed out of their controlled orbits by natural perturbations due to gravity and radiation pressure.

According to a report by the European Space Agency, an estimated 54,000 space debris objects larger than 10 cm and about 1.2 million space debris objects larger than 1 cm were orbiting the Earth as of August 2024[2]. While the size of these particles may seem small, each of them could be traveling with a relative velocity to other spacecraft of 30,000 km/hour, resulting in potentially severe damage should a collision occur (Mark & Kamath, 2019). As stated by the Kessler syndrome, proposed in 1978, the probability of collisions between space debris is continuously increasing, as broken pieces from these

[1] IADC Space Debris Mitigation Guidelines, Rev 4 (2025), last accessed: 29 March 2025
[2] European Space Agency Annual Space Environment Report (2025), last accessed: 18 April 2025

accidents take on uncontrollable trajectories that may lead to more accidents (Kessler & Cour-Palais, 1978).

Unfortunately, even with the growing risks, as with many aspects of space exploration, the development of international regulations on space debris has been relatively slow in comparison to the advancements in the industry. It has been widely noted that a significant portion of laws regarding space arise from non-binding agreements that generally transition into customary laws after long periods of time (Jankowitsch, 2015). Rules for managing non-functional devices were not included in the United Nations' (UN) "Outer Space Treaty" of 1967, though there was a strong emphasis on collaboration to protect the global ability to safely conduct space exploration[3]. Stricter guidelines concerning the registration of and liability for objects launched into space were not implemented by the UN until the 1970's[4]. While the UN has continued to put out policies to protect the space environment, the adoption of these guidelines varies internationally, as some countries either do not belong to the organization or have not ratified the aforementioned treaties into law.

That being said, the IADC recognizes two protected regions in the guidelines for its members to mitigate their space debris impact: low Earth orbits (LEO) of under 2000 km in altitude and the geostationary orbit (GEO) region between 33,786 km and 37,786 km of altitude[5]. Notably, satellites in medium Earth orbit (MEO) are excluded from these protections, some of which belong to Global Navigation Satellite Systems (GNSS). For the Global Positioning System (GPS), Global'naya Navigatsionnaya Sputnikovaya Sistema (GLONASS), BeiDou, and Galileo constellations, MEO space is invaluable, as their specialized orbits allow them to provide global navigation capabilities to their respective users (Teunissen & Montenbruck, 2017).

The method of disposal for defunct satellites in each of these regions varies, with de-orbiting procedures being a popular option for LEO devices. De-orbiting is a process where the device's velocity is slowed enough to lower its orbit into the Earth's atmosphere until it eventually burns up.

[3] Outer Space Treaty of 1967, last accessed: 29 March 2025
[4] United Nations Space Law Treaties and Principles, last accessed: 29 March 2025
[5] See footnote 1

For MEO, GEO, and other high-altitude satellites, however, de-orbiting can be too expensive and time-consuming. In these cases, the use of so-called graveyard orbits to dispose of dead or broken spacecraft is the more appealing option, as it consists of transferring the device to an orbit of higher or lower altitude such that the natural perturbations on the debris will take an extended period of time to push it back. Many GEO satellites are placed into graveyard orbits of even higher altitudes in an end-of-life procedure so as not to interfere with the geostationary transfer orbits, a process adopted by the European Space Agency in 1989 (Flury, 1991). MEO GNSS satellites, on the other hand, have semi-major axis values ranging between 25,510 km for the GLONASS and 29,600 km for the Galileo constellations, respectively (Teunissen & Montenbruck, 2017). These satellites are thus either sent into graveyard orbits with higher or lower altitudes of around 500 km, depending on their initial positions.

However, there are concerns over the environmental and economic costs of using fuel as a propellant to conduct orbital transfers to graveyard orbits and de-orbiting procedures. Furthermore, as will be discussed in detail in Section 2.3.2, certain resonance effects in the GNSS orbital space have the potential to cause collisions between non-functional and functional satellites. As it turns out, capitalizing on the natural perturbations that disturb uncontrollable space debris may be the solution to the space pollution problem.

## 1.2 Solar Radiation Pressure and Solar Sails

Objects orbiting the Earth experience several non-conservative perturbations, and for those with altitudes exceeding 800 km, radiation pressure from the Sun becomes the driving non-conservative force (Vokrouhlicky et al., 1993). Although the photons radially emitted from the Sun are massless, they have energy and momentum. When these massless particles are absorbed or reflected on an object's surface, their impulse is transferred to the object (Montenbruck & Gill, 2000). The force exerted onto the object's surface due to this momentum exchange is commonly known as Solar Radiation Pressure (SRP), a phenomenon which has been the subject of scientific theory since 1619, when Johannes Kepler hypothesized that pressure from sunlight was responsible for pushing comet tails outwards from the Sun (McInnes, 1999). It wasn't until 1900, however, that radiation pressure was experimentally proven to exist and measured by Pyotr Lebedev (Masalov, 2019).

While some scientists such as Konstantin Tsiolkovsky and Carl Wiley presented early theories on how to harness this natural perturbation to propel or even control spacecraft in the decades that followed its discovery (McInnes, 1999), widespread interest in the relationship between SRP and the behavior of artificial satellites didn't take hold until the 1960's. During this time, many preliminary studies were conducted, including the first measurement of solar pressure by a spacecraft, which was taken by the National Aeronautics and Space Administration's (NASA) Echo I balloon (Bryant, 1961; Muhleman et al., 1960; Johnson et al., 2012). One such study included derivations that, upon examination, indicated that over one period where the satellite does not travel through an eclipse, the long-term perturbations in the semi-major axis will average out, though this will not occur if the spacecraft passes through a shadowed region (Kozai, 1963; Vokrouhlicky et al., 1993). In essence, if a spherical satellite experiences an eclipse during part of its orbit, there will eventually be changes in the semi-major axis values that cannot be attributed to atmospheric drag or gravitational perturbations. Furthermore, as the acceleration due to SRP is directly proportional to an object's area-to-mass ratio, its effect on larger, lightweight spacecraft will be more pronounced, whereas it can be considered negligible for smaller objects with comparatively larger mass values (Junshou et al., 2014). The optical parameters of the surface on which the photons impinge are also a consideration, as higher momentum transfers occur when the photons bounce off of highly reflective objects.

The principle of leveraging high area-to-mass ratios and surface reflectivity to harness SRP as a propellant soon gave way to the development of the traditional solar sail. Solar sails, in their most basic form, are extremely thin, highly reflective membranes that maximize the area-to-mass ratio of a spacecraft to continuously accelerate using SRP rather than fuel. The membrane is often held taut using booms, or deployable arm-like structures. The first successful deployment of a solar sail for interplanetary travel was conducted by the Japan Aerospace Exploration Agency in 2010, when the Interplanetary Kite-craft Accelerated by Radiation Of the Sun (IKAROS) probe performed a successful fly-by of Venus using photon propulsion (Mori et al., 2014).

Following the success of this invention, the industry surrounding solar sails has expanded. The emergence of the CubeSat- small cubic satellites with edges in units of 10 cm (1U) or more that typically consists of commercial off-the-shelf components- as a competitive solution for low-cost satellite missions has branded it as a viable bus for many solar sail technologies (Villela et al., 2019; Lantoine et al., 2024; Lappas et al., 2011; Johnson et al., 2012). As fuel-less, continuous sources of small thrust in an environment with no air resistance, solar sails have been the focus of many ideas for accelerating long-term and interplanetary probes (Nassiri et al., 2005; Mori et al., 2014). While this has long been one of the most prominent ideas associated with solar sails (McInnes, 1999), there have also been significant developments in research targeted toward using SRP to clean up the orbits around Earth (Arshad et al., 2025).

Several experiments have been performed to explore the use of SRP to guide LEO satellites into atmospheric re-entry. In 2011, the Nanosail-D2 3U CubeSat mission successfully deployed and used a 10 m$^2$ sail in LEO conditions to perform a de-orbiting maneuver using atmospheric drag (Zhao et al., 2023), demonstrating the viability of this technology through the end of the disposal process. Furthermore, the ability to control a satellite's trajectory and increase the rate of orbital decay while in orbit around Earth using pressure from the sunlight has been proven by the LightSail-2 solar sail, which operated in a near-polar orbit for several years (Spencer et al., 2021).

Other studies geared toward increasing the sustainability of space focus on sending GEO satellites into graveyard orbits through the use of solar sails (Carvalho et al., 2023; Silva Neto et al., 2017). Graveyard orbits, however, are essentially a non-renewable resource, as once they become over-polluted with debris, there may not be a way to clear them. As a result, it becomes increasingly more important to identify and develop new disposal methods for space debris and non-functional satellites in MEO.

## 1.3 Spherical Solar Sails

While traditional solar sails offer a clean energy solution, the process can be challenging, as it can be hard to achieve and maintain the target attitude. The orientation of flat solar sails is extremely important, as the angle between the radiation pressure and the sail membrane dictates the magnitude and orientation of the resulting acceleration due to SRP (Zhang et al., 2022).

One of the most notable advantages of using a spherical solar sail as a de-orbit device is the elimination of attitude adjustments to keep the sail properly oriented, as the resultant force vector from the SRP on the sphere will always follow the Sun-satellite line. This is due to the symmetry of the sail, as all of the tangential components of acceleration cancel each other out, which also results in no generation of solar pressure torques, as seen with the Echo II balloon in 1964[6].

For the purposes of this study, it is assumed that the balloon and satellite bus are together one perfectly spherical shape of uniform reflectivity, meaning the acceleration due to SRP is not dependent on the orientation of the spacecraft. Under this assumption, the spin of the device in orbit is negligible. The magnitude of the perturbative force will instead be controlled by inflating and deflating the balloon to alter its area-to-mass ratio as needed. This idea of altering the area-to-mass ratio of an artificial balloon to dictate the satellite's trajectory has been explored by previous studies with varying model complexity (Deienno et al., 2016; Guerman and Smirnov, 2012; Krivov and Getino, 1997). Furthermore, inflatable mechanisms are popular for in-space use due to their relatively light weight and small initial volume, which cut launch costs by reducing the level of fuel and space needed to launch them into orbit (Zhao et al., 2023).

In the proposed model, the balloon's size will be systematically increased and decreased until the satellite is pushed it into lower altitudes, where it will eventually burn up in the Earth's atmosphere upon re-entry. An exaggerated version of the resulting orbit from this process is shown in Figure 1.1. When approaching the Sun, and thus, traveling against the SRP, the balloon should be fully inflated, maximizing the satellite's area-to-mass ratio. As the solar perturbation acts against the satellite's motion, it will experience a slight decrease in its velocity, increasing the eccentricity and causing a general decrease in the semi-major axis of the orbit over time. In Figure 1.1, an exaggeration of this loss is visibly shown on the right side of the plot, as the satellite does not have the energy required to loop back to its initial position. While traveling away from the Sun, the balloon should be fully deflated to minimize the pushing effect of the SRP perturbations. Otherwise, any energy and velocity lost while the device travels against the flow of SRP

[6] Solar Sail Model Validation from Echo Trajectories, last accessed: 3 April 2025

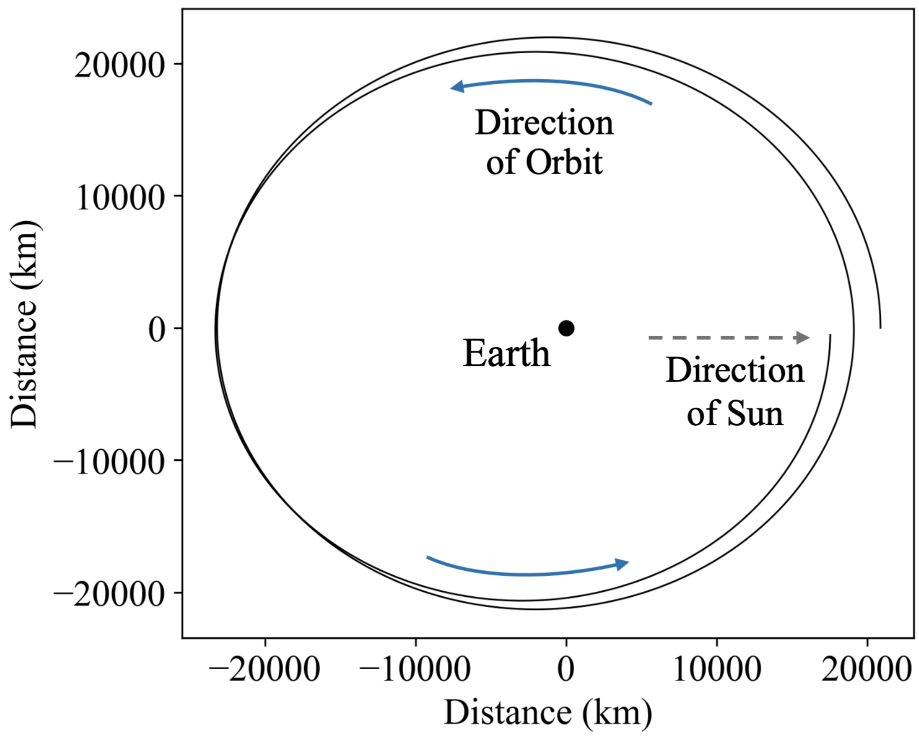


FIGURE 1.1: Exaggerated example of the energy loss due to the deployment of a balloon with an adjustable area-to-mass ratio experiencing acceleration due to SRP. The satellite's counter-clockwise trajectory around the Earth is displayed.

would be regained during this time, and the satellite would return much closer to its initial position.

While the proposed inflatable, reflective sphere could be installed onto new satellites and deployed during the end-of-life mission phase, there is also the potential to create a space tug specifically designed to capture and de-orbit existing space debris. The process outlined in Figure 1.1 could theoretically be reversed, should the balloon be inflated when traveling in the direction of the SRP, and deflated when flying against it. Thus, a cycle of capturing space debris, harnessing SRP to slow its velocity until it can be deposited at the point atmospheric drag takes effect, and reversing the inflation and deflation processes to re-enter the graveyard orbits for more debris can be initiated.

The goal of this research is, therefore, to model the orbit of a device that harnesses SRP as a de-orbiting method to mimic real-world behaviors. The feasibility of the proposed inflatable, spherical solar sail to push MEO satellites back into the Earth's atmosphere is gauged. Both instantaneous and linear inflation and deflation processes are described and tested for various inclinations and other initial conditions. Another goal of this study is to identify the best-case scenario within the constraints of the model to conduct the re-entry process based on inflation and deflation rates, orbital inclinations, and other parameters.

## 1.4 Thesis Overview

This research document is organized as follows:

- Chapter 2: A description of the dynamical model is given. Equations of motion and relevant perturbations for each major body are defined. Calculation methods for perturbations due to third bodies, Earth's spherical harmonics, atmospheric drag, and SRP are also provided. The cannonball and shadow models used in SRP calculations are explained, and justifications for selected values of the reflectivity coefficient, area-to-mass ratios, inclination, and other initial orbital elements are listed. The behaviors of the fully deflated and inflated balloon are analyzed.

- Chapter 3: The numerical setup of the model is outlined, including the selection of specialized Python packages, ordinary differential equation solvers, and sources of imported parameters for major bodies.

- Chapter 4: The methodology behind tracking the satellite's trajectory with respect to the SRP is defined. Then, the binary inflation and deflation processes are explained, and the impact of reflectivity on the system is explored. The processes of linear inflation and deflation are then outlined, and the ideal time frame for each of these procedures is identified.
- Chapter 5: The best-case scenarios for realistic de-orbit processes are modeled and discussed. A case study using GPS satellite orbit conditions is then performed. Potential materials for the balloon and parameters for a gas compressor are established.
- Chapter 6: A summary of the research is presented, and recommendations for future analysis and development of the model are given.
- Chapter 7: A link to the GitHub page containing all files used to run the model is provided.

# Chapter 2

# Dynamic Model

The model utilized in this research tracks the effects of SRP on an Earth-orbiting satellite outfitted with an inflatable, spherical solar sail. The model consists of an Earth-Sun-Moon-satellite system, with the approximated center of Earth acting as the origin, and an epoch of January 1st, 2025. Parameters for major bodies such as rotational speed, mean and equatorial radius, mass, standard gravitational parameter, and obliquity of the ecliptic were pulled from the Jet Propulsion Laboratory (JPL) Horizons database[1], the 2024 Astronomical Almanac, and NASA's National Space Science Data Center[2] (Office et al., 2023).

## 2.1 Equations of Motion

The satellite, Moon, and Sun require equations of motion (EOMs) to calculate the changes in their orbits with respect to the Earth, which is the origin of the system. These equations consider several perturbations when appropriate, including third-body perturbations, effects of the Earth's spherical harmonics and oblateness, acceleration due to SRP, and atmospheric drag.

### 2.1.1 Sun Equation of Motion

The Sun's EOM was found by considering the Sun as part of a three-body problem with the Earth and the satellite. The motion of the Sun, $\odot$, relative to the Earth, $\oplus$, can thus be

[1] JPL Horizons database, last accessed: 25 March 2025
[2] NASA Planetary fact sheets, last accessed: 22 March 2025

expressed as:

$$\ddot{\mathbf{r}}_{\odot} = \frac{d^2 r_{\odot}}{dt^2} = \frac{-(\mu_{\odot} + \mu_{\oplus})\mathbf{r}_{\odot}}{r_{\odot}^3} \tag{2.1}$$

where $\mathbf{r}_{\odot}$ is the position vector of the Sun and $\mu_{\odot}$ and $\mu_{\oplus}$ are the standard gravitational parameters of the Sun and Earth, respectively.

### 2.1.2 Moon Equation of Motion

The EOM for the Moon, ☾, included several additional perturbations due to the Earth's spherical harmonics and the Sun's presence in the system:

$$\ddot{\mathbf{r}}_{☾} = \frac{d^2 r_{☾}}{dt^2} = \frac{-(\mu_{☾} + \mu_{\oplus})\mathbf{r}_{☾}}{r_{☾}^3} + \mathbf{a_{J_2}} + \mathbf{a_{3B_{\odot}}} \tag{2.2}$$

where $\mathbf{r}_{☾}$ is the position vector of the Moon, $\mu_{☾}$ is the standard gravitational parameter of the Moon, $\mathbf{a_{J_2}}$ is the acceleration due to spherical harmonic perturbations, and $\mathbf{a_{3B_{\odot}}}$ is the third-body acceleration due to the Sun.

Due to the Moon's distance from the Earth, the only perturbation from the Earth's spherical harmonics of note will be the planet's oblateness. Thus, only the second zonal harmonic of Earth, $J_2$, was used to account for the planet's spherical harmonics:

$$\mathbf{a_{J_2}} = \frac{1.5 J_2 \mu_{\oplus} R_e \mathbf{r}_{☾}}{r_{☾}^2} \left[ \left( \frac{5 r_{☾,z}^2}{r_{☾}^2} - 1 \right) \hat{i} + \left( \frac{5 r_{☾,z}^2}{r_{☾}^2} - 1 \right) \hat{j} + \left( \frac{5 r_{☾,z}^2}{r_{☾}^2} - 3 \right) \hat{k} \right] \tag{2.3}$$

where $R_{\oplus}$ is the mean equatorial radius of Earth.

#### Third-Body Perturbations

The Moon's EOM also includes a third-body perturbation from the Sun. Third-body perturbations describe the acceleration due to the attractive gravitational force of additional objects in the system, and are generally calculated using:

$$\mathbf{a_{3B_d}} = \mu_d \left( \frac{\mathbf{r_{s,d}}}{r_{s,d}^3} - \frac{\mathbf{r_d}}{r_d^3} \right) \tag{2.4}$$

where the acceleration due to this perturbation is $\mathbf{a_{3B_d}}$, the disturbing body is $d$, which has a standard gravitational parameter of $\mu_d$, the disturbed object is $s$, and the perturbation is acting along the vector pointing from the disturbed object to the disturbing body:

$$\mathbf{r_{s,d}} = \mathbf{r_d} - \mathbf{r_s} \tag{2.5}$$

where $\mathbf{r_d}$ and $\mathbf{r_s}$ are the position vectors of the disturbing body and disturbed object, respectively. This perturbation in the Moon's EOM was calculated by setting the Sun as the disturbing body and the Moon as the disturbed object.

### 2.1.3 Satellite Equations of Motion

The EOM for the satellite was defined in the model as:

$$\ddot{\mathbf{r}}_{\mathbf{sat}} = \frac{d^2 r_{sat}}{dt^2} = \frac{-\mu_{\oplus}\mathbf{r_{sat}}}{r_{sat}^3} + \mathbf{a_{3B_{\odot}}} + \mathbf{a_{3B_{☾}}} + \mathbf{a_{EGM}} + \mathbf{a_{atm}} + \mathbf{a_{SRP}} \tag{2.6}$$

where $\mathbf{r_{sat}}$ is the position vector of the satellite, and the first term describes the acceleration due to gravity between the Earth and the satellite. This equation also includes the third-body perturbations from the Sun, $\mathbf{a_{3B_{\odot}}}$, and the Moon, $\mathbf{a_{3B_{☾}}}$, on the satellite. The last three terms, $\mathbf{a_{EGM}}$, $\mathbf{a_{atm}}$, and $\mathbf{a_{SRP}}$, are the perturbations due to the Earth Gravitational Model, atmospheric drag, and SRP, respectively.

#### Earth's Spherical Harmonics

For the Earth-orbiting satellite, there will be an acceleration due to the gravity field of the Earth that depends on the planet's spherical harmonics, given by $\mathbf{a_{EGM}}$. The model is equipped to calculate this perturbation using the standard forward column method found in (Holmes & Featherstone, 2002) and normalized spherical harmonics coefficients up to degree and order 2,198, found in the 2008 Earth Gravitational Model database [3]. For the purposes of this research, the model was set to consider an order of zero and a degree of two.

[3] National Geospatial-Intelligence Agency Office of Geomatics EGM2008, last accessed: 18 March 2025

**Atmospheric Drag**

The model takes the acceleration due to atmospheric drag on the satellite, $\mathbf{a_{atm}}$, into account when its radius is less than of equal to 900 km, and employs a constant drag coefficient value of 2.2 for simplicity, as is common for many LEO satellite models(X. Wang et al., 2024). The atmospheric density model was pulled from the 1976 U.S. Standard Atmosphere model[4]. The dynamic model also referenced other sources to develop the exponential variation of the atmosphere (King-Hele, 1987), the static model (Jacchia, 1977), and the calculation of velocity components with respect to the atmosphere (Vallado & McClain, 2007). Although atmospheric drag is an active perturbation for altitudes up to 1000 km (Curtis, 2021), it has been shown that the acceleration due to atmospheric drag at altitudes of 900 km, while still present in the system, is about five times smaller than that of direct solar radiation pressure (Krzysztof, 2015). However, at altitudes of 800 km or less, this drastically changes, with atmospheric drag taking on a much larger role in the satellite's EOM (Krzysztof, 2015; Vokrouhlicky et al., 1993). While these values were calculated for satellites with smaller area-to-mass ratios than the fully inflated satellite, the accelerations due to SRP and drag are both proportional to this ratio, meaning the comparison can be reasonably applied to satellites with higher or smaller area-to-mass values. It should thus be emphasized that the behavior of the satellite harnessing SRP at altitudes under 900 km is not within the scope of this research, as it would be difficult to separate the effects due to SRP from the perturbations due to drag.

## 2.2 Solar Radiation Pressure Calculations

In order to most accurately calculate the perturbation due to SRP on the satellite, $\mathbf{a_{SRP}}$, the dynamic model uses the traditional cannonball model from (Curtis, 2021), assuming the satellite to be a perfect sphere of radius $R_{sc}$. This yields an apparent area of:

$$A_{sc} = \pi R_{sc}^2 \tag{2.7}$$

[4] U.S. Standard Atmosphere, 1976, last accessed: 27 March 2025

The solar radiation pressure $P_{SR}$, also known as the momentum flux, was found by dividing the solar constant $S$, also known as the radiation intensity, by the speed of light, $c$:

$$P_{SR} = \frac{S}{c} \tag{2.8}$$

While the cannonball model uses the position vector from the Sun to the Earth to calculate the acceleration due to SRP on Earth-orbiting spacecraft, as one auxiliary unit is significantly larger than the radius of the orbiting satellite, the model does not. Instead, to increase precision, the position vector pointing from the satellite toward the Sun was used:

$$\mathbf{r_{sat,\odot}} = \mathbf{r_{\odot}} - \mathbf{r_{sat}} \tag{2.9}$$

while the magnitude of this vector was found to calculate the value of the radiation intensity at the satellite:

$$S = S_0 \left( \frac{R_0}{r_{sat,\odot}} \right)^2 \tag{2.10}$$

where $S_0$ is the radiated power intensity at the visible surface of the Sun, known as the photosphere, and $R_0$ is the radius of the photosphere. A negative sign was used to reverse the direction of the $\hat{r}_{sat,\odot}$ unit vector to calculate the perturbing acceleration on the satellite:

$$\mathbf{a_{SRP}} = -\frac{\nu P_{SR} C_R A_{sc}}{m_{sc}} \hat{r}_{sat,\odot} \tag{2.11}$$

where $\nu$ is the shadow function, $m_{sc}$ is the mass of the satellite, and $C_R$ is the reflectivity coefficient. This value was calculated using the solar sail material's reflectivity, $\varepsilon$:

$$C_R = 1 + \varepsilon \tag{2.12}$$

and ranges between 1 and 2, with a coefficient of 1 indicating a blackbody (Montenbruck & Gill, 2000). Conversely, a coefficient of 2 will yield double the force on the spacecraft, as it indicates the total reflection of incident radiation (Curtis, 2021). The magnitude of the perturbation is therefore directly proportional to the reflectivity coefficient of the sail material and the area-to-mass ratio of the satellite. It is assumed that the entirety of the theoretical cannonball is composed of the sail material.

### 2.2.1 Shadow Model

The shadow function in the model determines whether or not the satellite is in a total or partial eclipse on the night side of the Earth, and was based off the conical shadow model found in (Montenbruck & Gill, 2000), as shown in Figure 2.1. This shadow model

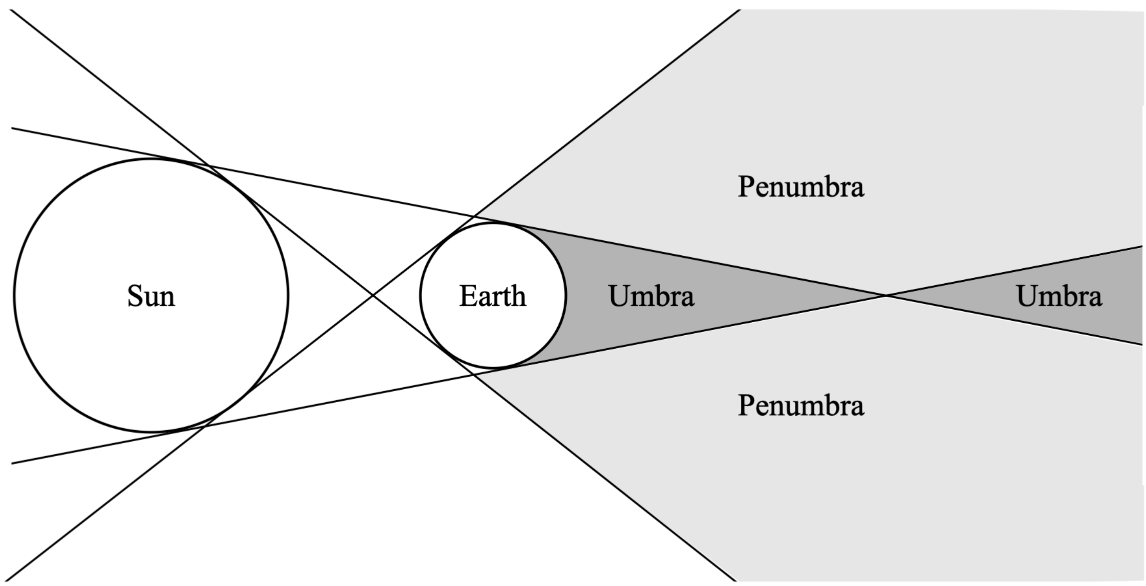


FIGURE 2.1: Conical shadow model demonstrating regions of total and partial eclipse

neglects the oblateness of the occulting body, which was Earth in this case, and designates the umbral shadow region as a total eclipse region, while the shadow function value in the penumbral cone varies. The Sun and Earth were treated as circular disks to calculate the degree of the Sun's occulation, as shown in Figure 2.2. The occulted area of the solar disk was calculated as:

$$A_{occ} = r_{app,\odot}^2 cos^{-1}\left(\frac{x}{r_{app,\odot}}\right) + r_{app,\oplus}^2 cos^{-1}\left(\frac{d_{app} - x}{r_{app,\oplus}}\right) - d_{app}y \tag{2.13}$$

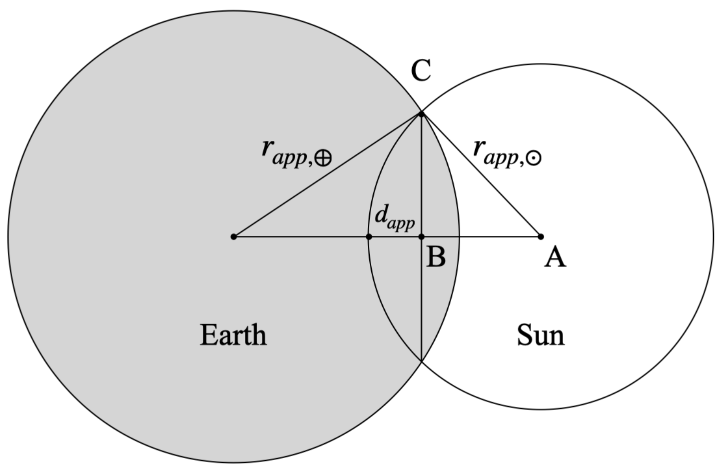


FIGURE 2.2: Occulation of the Sun by the Earth using apparent radii and distance

where the $x$ and $y$ values are the distances $\overline{AB}$ and $\overline{BC}$ in Figure 2.2. The apparent radius of the Sun, $r_{app,\odot}$, was given by:

$$r_{app,\odot} = sin^{-1}\left(\frac{R_\odot}{r_{sat,\odot}}\right) \tag{2.14}$$

where $R_\odot$ represents the Sun's volumetric mean radius. The apparent radius of the Earth was similarly calculated as:

$$r_{app,\oplus} = sin^{-1}\left(\frac{R_\oplus}{r_{sat}}\right) \tag{2.15}$$

where $R_\oplus$ represents the Earth's volumetric mean radius and the apparent separation between the centers of the disks, $d_{app}$, was found using:

$$d_{app} = cos^{-}1\left(\frac{-(\mathbf{r_{sat}} \cdot \mathbf{r_{sat,\odot}})}{r_{sat} r_{sat,\odot}}\right) \tag{2.16}$$

Finally, the shadow function value, $\nu$, which ranges from 0 to 1 for total eclipse to total sunlight values, respectively, was calculated:

$$\nu = 1.0 - \frac{A_{occ}}{\pi r_{app,\odot}} \tag{2.17}$$

### 2.2.2 Reflectivity Coefficient

As mentioned previously, the reflectivity coefficient of the solar sail material is directly proportional to the acceleration due to SRP experienced by the spacecraft. Thus, the selection of the proper solar sail material will have a large impact on the balloon's performance. For the purposes of this study, it was decided to use aluminum-coated Mylar as the balloon material. Mylar laminates are a popular material for solar sail construction and have been used with aluminum foil to create inflatable spherical spacecraft, as seen with Echo II in 1964[5]. In the research conducted for NASA's prospective solar sail mission to Halley's Comet (McInnes, 1999), it was determined that vapor-deposited aluminum coatings would produce a spectral reflectance between 0.88 and 0.91 on a scale

[5] NASA Space Science Data Coordinated Archive: Echo II, last accessed: 10 March 2025

from 0 to 1, with 0 indicating a blackbody with total absorption of incident electromagnetic radiation (Rowe, 1978). A study looking to update the NASA solar sail thrust model also found that due to aluminum's "opaque optical thickness," this range of reflectivity values may be considered for any sail material with an aluminum coating of at least 100 nm (Heaton & Artusio-Glimpse, 2015). While the optimal solution would be to use a reflectivity of 0.91 to increase the effects of SRP, in order to align with more recent publications (Montenbruck & Gill, 2000), a reflectivity coefficient of 1.88 was used in all trials unless otherwise stated.

## 2.3 Fully Deflated and Inflated Balloon Behavior

Before conducting trials with inflation and deflation methods, the modeled behavior of the fully deflated and inflated balloon was analyzed. As previously discussed, the parameters for this de-orbiting technology model are meant to emulate GNSS satellites in low-altitude graveyard orbits. Thus, an initial semi-major axis of 22,000 km was used in all trials unless otherwise stated, yielding an MEO with an initial altitude of 15,621.86 km. While this semi-major axis value is lower than that of the expected GNSS graveyard orbits (Teunissen & Montenbruck, 2017), it was chosen to both avoid resonances that could overshadow the effects of SRP and to cut computation times. As an initial eccentricity value of 0 would cause other orbital elements to become undefined when calculated, it was decided to model a near-circular orbit with an initial eccentricity of 0.05. The initial values of the argument of the perigee, right ascension of the ascending node, and mean anomaly were all set to 0 degrees, as they do not present the same resulting errors in calculation as the eccentricity does.

### 2.3.1 Area-to-Mass Ratio

For the purposes of this study, the model was set to consider area-to-mass ratios of 0.04 $m^2/kg$ for a fully deflated balloon and 1.0 $m^2/kg$ for a fully inflated balloon. These values are well within the range of acceptable area-to-mass ratios for a spherical solar sail, as NASA's Echo 1, Echo 2, and Pageos balloons- each a reflective, thin-walled communications satellite- were deployed with area-to-mass ratios on the order of 10 $m^2/kg$ back in the 1960s (Curtis, 2021). Furthermore, the IKAROS probe had an area-to-mass ratio of 0.638 $m^2/kg$, which is within the range of selected values (Mori et al., 2014). The selected mass of the satellite was 100.0 kg, which should be sufficient to account for the balloon, compressor, compressed inflation gas, and other equipment.

### 2.3.2 Inclination

Four notable inclination values were used to represent the full range of possible orbit inclinations. For example, GEO satellites, such as those used for telecommunications, have orbits in the equatorial plane (Spaelti et al., 1989). Although GEO satellites are not the focus of this study, an inclination of 0.001 degrees was used to model the behavior of satellites in equatorial orbits at smaller altitudes. Conversely, an inclination of exactly 0 degrees, while more accurate, would present computational errors in the model. Other notable inclinations modeled were 23.44 degrees, or the inclination of the Earth's ecliptic plane[6], and 90 degrees to model polar orbits. Spacecraft with retrograde orbits can also be modeled; however, as their trajectories are mirror images of prograde orbits, no retrograde orbits are included in the analysis.

The final inclination to be modeled allows us to estimate the effectiveness of the spherical sail in GNSS orbits where a special resonance occurs. Both GPS and Galileo constellations operate at inclinations of 56 degrees, while BeiDou uses a 55-degree inclination and GLONASS orbits at approximately 64.8 degrees (Teunissen & Montenbruck, 2017). In cases where the effects of oblateness become dominant, such as for objects orbiting close to the Earth, the following resonance is present at an inclination of 56.06 degrees:

$$2\dot{\omega} + \dot{\Omega} \approx 0 \tag{2.18}$$

where $\dot{\omega}$ and $\dot{\Omega}$ are the first time derivatives of the argument of perigee and the longitude of the ascending node (Sanchez et al., 2009). When the Sun is considered a third-body disturber in the system, this resonance causes a sharp increase in the satellite's eccentricity over time (Sanchez et al., 2009; Alessi et al., 2017). This resonance is a particular problem when considering the debris and non-functional satellites in the GNSS graveyards, as it

[6] NASA Earth fact sheet, last accessed: 22 March 2025

can slowly alter their trajectories until they cross back into the operating orbits, potentially causing collisions with the current systems.

The behavior of the fully deflated balloon's eccentricity at each of these inclinations was thus explored, as shown in Figure 2.3.

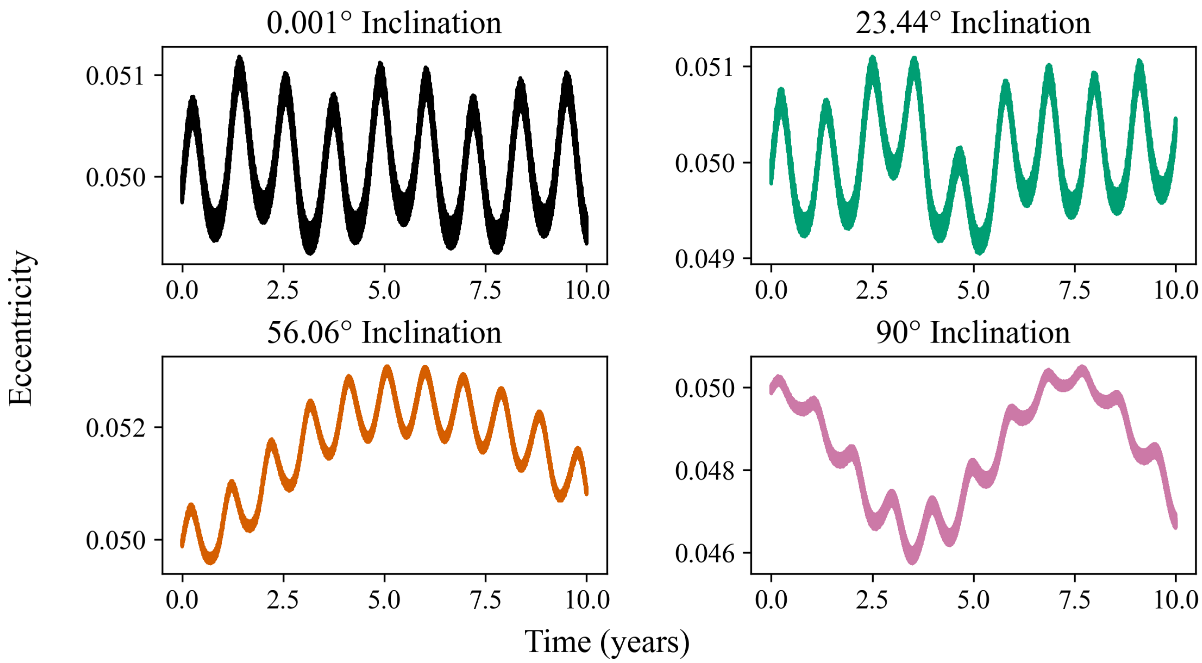


FIGURE 2.3: Eccentricity over 10 years of a fully deflated balloon with initial inclination values of 0.001 (top left), 23.44 (top right), 56.06 (bottom left), and 90.0 degrees (bottom right) and initial value of 0.05 for eccentricity.

Although the eccentricity reaches a higher maximum value in the 56.06-degree test than in the other trials, it should be noted that the eccentricity for near-circular orbits at this inclination will follow a bell-curve shape due to the aforementioned resonance, with a peak value occurring after around 600 years (Sanchez et al., 2009). As the time frame for the trials in Figure 2.3 is only 10 years, the dominance of this resonance will actually keep the eccentricity at relatively low values.

Out of all of the trials, the near-equatorial inclination of 0.001 degrees presents the most homogeneous trend of oscillation, as the 23.44-degree trial shows a sharp dip in the maximum eccentricity at around 4.4 years, and the polar orbit presented both small and large periodic sinusoidal trends. The changes in the semi-major axis values of the balloon for each inclination value are shown in Figure 2.4. As seen in Figure 2.4, the semi-

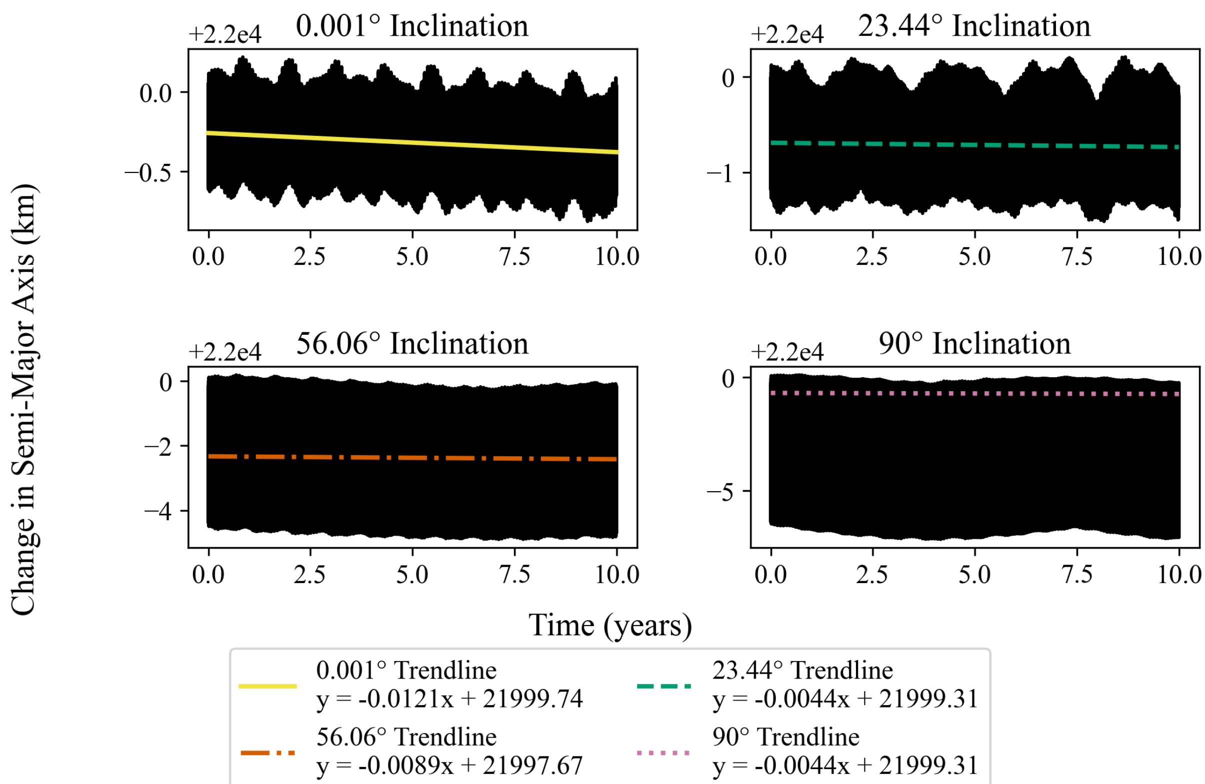


FIGURE 2.4: Behavior and trend lines of the semi-major axis in km over 10 years for a fully deflated balloon with initial inclination values of 0.001 (top left), 23.44 (top right), 56.06 (bottom left), and 90.0 degrees (bottom right) and initial semi-major axis of 22,000 km.

major axis value slightly fluctuates for all inclinations tested. This expected behavior is caused by the presence of perturbations in the EOMs, which were described in the previous section. A closer look at the semi-major axis behavior for the fully deflated balloon at an inclination of 0.001 degrees is shown in Figure 2.5.

While the semi-major axis in Figure 2.5 experiences a drop of 0.6 km each period, it rises back to a slightly higher point than its initial value of 22,000 km. As shown in Figure 2.4, this trend of a slightly increasing semi-major axis value at the start of the 0.001-degree orbit eventually transitions into a long-term decline in the range of semi-major axis values according to the trend line. This long-term behavior is mimicked for all inclinations in

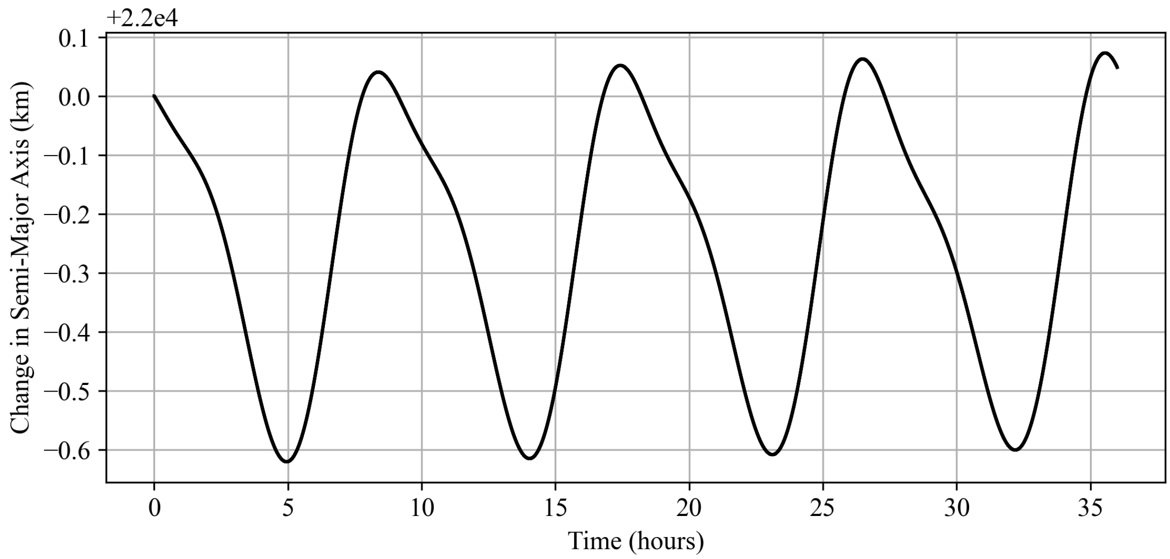


FIGURE 2.5: Change in semi-major axis values in km of a fully deflated balloon over 36 hours.

Figure 2.4, though their short-term periodic behaviors vary. Interestingly, the closer each orbit is to being polar, the smoother the short-term periodic changes become.

### 2.3.3 Fully Inflated Balloon Behavior

Another point of interest that should be addressed is how the satellite's behavior changes when the balloon is fully inflated for long periods of time. Thus, the semi-major axis values for a fully deflated and inflated balloon over 10 years with initial inclinations of 0.001 degrees were plotted against each other in Figure 2.6. While the semi-major axis values fluctuate and generally decrease for the fully deflated balloon, the range of values remains generally homogeneous over the 10-year period. Conversely, the fully inflated balloon experiences periods of increasing and decreasing semi-major axis values. This stark difference in appearance between the graphs is likely due to the dominance of the SRP perturbation in the inflated balloon's EOM. Because the deflated balloon has a minimal area-to-mass ratio, it will mostly be affected by perturbations due to gravity and spherical harmonics.

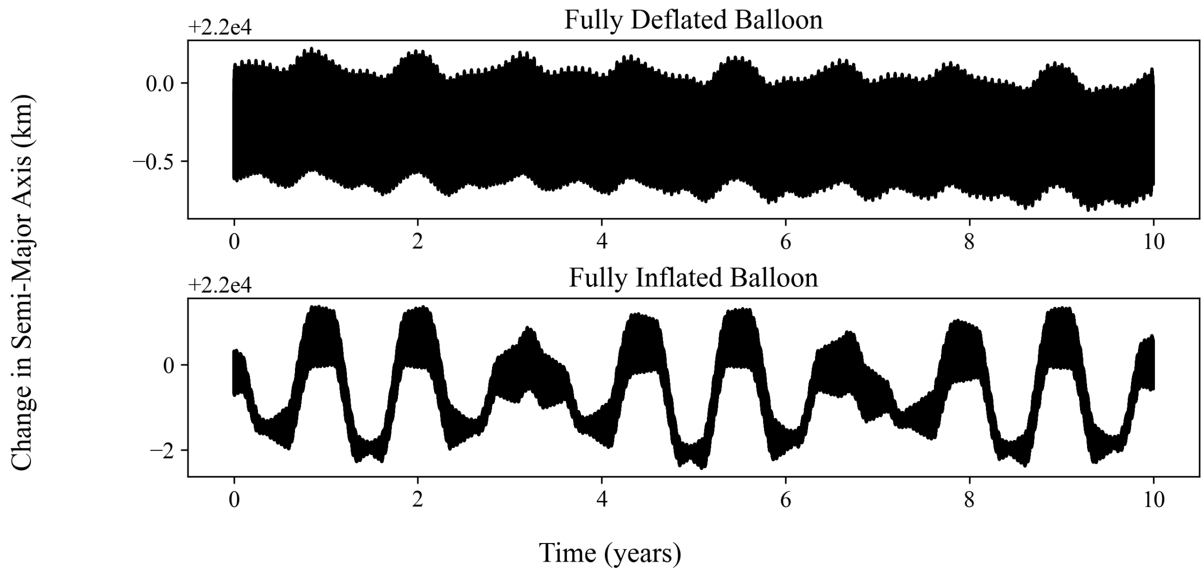


FIGURE 2.6: Change in semi-major axis in km over 10 years for a fully deflated (top) and fully inflated (bottom) balloon.

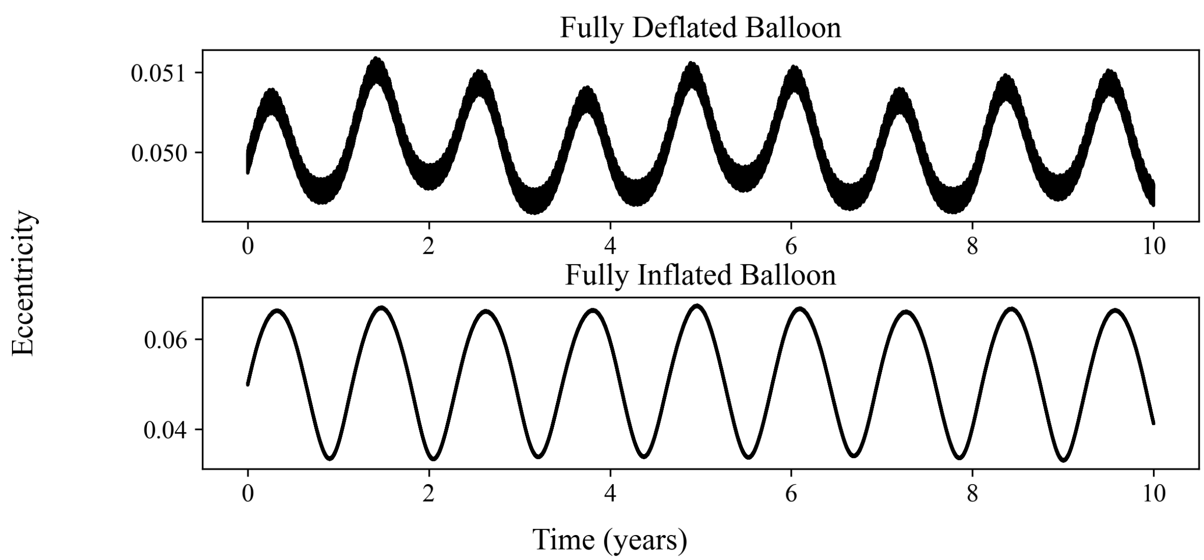


FIGURE 2.7: Eccentricity over 10 years for a fully deflated (top) and fully inflated (bottom) balloon.

The eccentricity values for the fully deflated and inflated balloons are also compared in Figure 2.7. As is expected, the peaks and troughs of the semi-major axis and eccentricity plots are out of phase with one another. Both plots display what appears to be a sinusoidal trend; however, the value of the eccentricity for the deflated balloon seems to fluctuate in small amounts along the orbit, while the amplitude of the eccentricity wave for the inflated balloon is much larger. These results are promising as they indicate that the SRP has a noticeable effect on the balloon and its orbital elements.

# Chapter 3

# Numerical Setup

The model was created in Python and uses geocentric arrays for the state vectors of the Sun, Moon, and satellite with respect to the Earth. Initial state vector information for each of the major bodies was extracted from the 2013 version of the JPL Horizons database[1]. To automatically pull the orbital elements for the selected epoch, the model imports Horizons from the astroquery.jplhorizons package[2].

The ordinary differential equations (ODEs) for each major body are then repeatedly solved to generate their updated positions and trajectories. To solve these ODEs, the solve_ivp function was imported from the scipy.integrate subpackage[3]. Then, a wrapper to the ODEPACK Fortran solver known as LSODA was selected as the integration method, as it automatically switches between the stiff backward differentiation formula and nonstiff Adams methods as needed (Hindmarsh, 1983; Petzold, 1983). This process allows for significantly shorter computation times and smoother results when compared to DOP853, an algorithm originally written for Fortran that is also compatible with the integrator (Hairer et al., 1993). The calculated area-to-mass ratios of the satellite using DOP853 and LSODA for the linear inflation and deflation of the balloon (which will be described in detail in Chapter 4) over a single period are compared in Figure 3.1. The advantages of using LSODA for the computations are clearly demonstrated in Figure 3.1, as there is a significant amount of noise during the inflation and deflation periods in the DOP853 trial.

[1] JPL Horizons database, last accessed: 25 March 2025
[2] JPL Horizons Queries, last accessed: 28 March 2025
[3] SciPy solve_ivp manual, last accessed: 28 March 2025

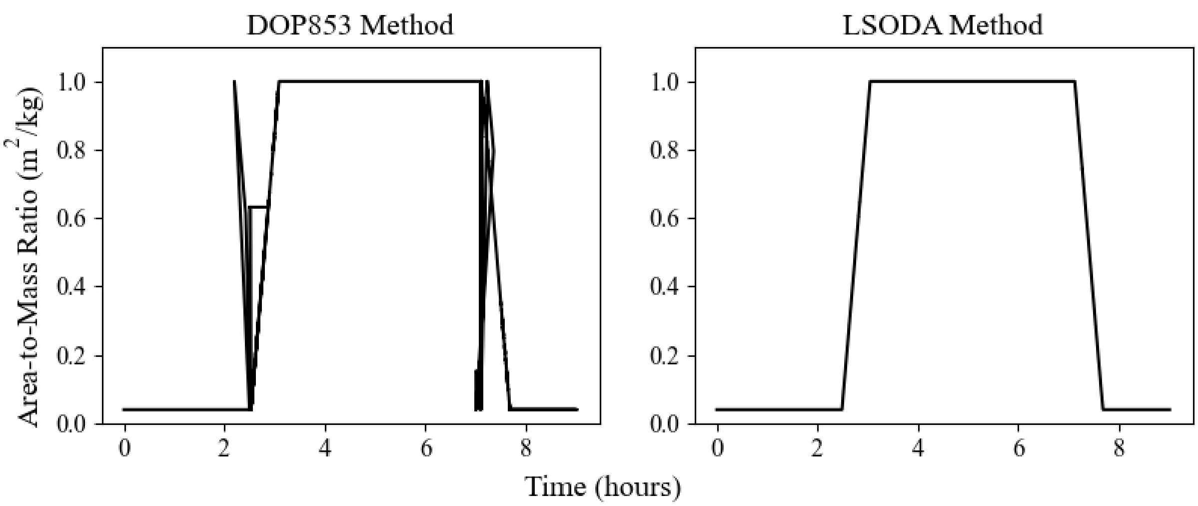


FIGURE 3.1: Area-to-mass ratio of the satellite over one period (about 9.0207 hours) using linear inflation and deflation for the DOP853 (left) and LSODA (right) integration methods.

# Chapter 4

# Methods of Harnessing Solar Radiation Pressure

## 4.1 Tracking the Satellite for Inflation and Deflation

While the model can derive the position of the satellite with respect to both the Earth and the Sun, as well as whether the device is within the Earth's shadow, predicting its trajectory presents a slightly more complicated problem. The solution chosen was to use the dot product between the direction of the SRP and the satellite's velocity, $\mathbf{v_{sat}}$, to determine if the device is approaching or going away from the Sun. Derived from the dot product equation, the cosine of the angle $\theta$ between these two vectors provides the model with an understanding of the satellite's trajectory:

$$cos(\theta) = \frac{\mathbf{r_{\odot,sat}} \cdot \mathbf{v_{sat}}}{v_{sat} r_{\odot,sat}} \tag{4.1}$$

Although the magnitude of the acceleration due to SRP on the satellite will be 0 when the satellite enters the Earth's shadow as per Equations 2.11 and 2.17, the cosine equation is not dependent on this value, and is thus able to track the satellite's position regardless of the shadow. As shown in Figure 4.1, the cosine value ranges from -1 at point B, when the satellite is traveling exactly opposite the SRP, to 1 at point D, when the satellite is traveling exactly along the Sun-satellite line. When the cosine is equal to 0 at points A and C, $\mathbf{v_{sat}}$ is perpendicular to the SRP.

For clarity, while the direction of SRP is notated as having a constant direction in Figure 4.1, the position vector from the Sun to the satellite is used for all cosine calculations

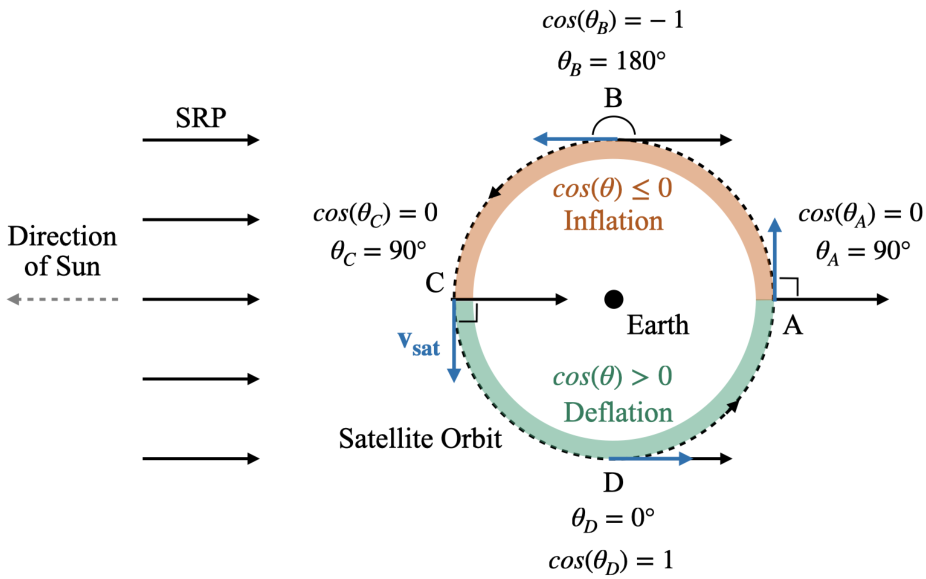


FIGURE 4.1: Cosine of theta values for the angle between various satellite trajectories and the SRP.

and may vary slightly in its angle.

## 4.2 Binary Inflation and Deflation

For binary inflation and deflation, the area-to-mass ratio flips between its minimum and maximum values depending on the sign of $cos(\theta)$. When $cos(\theta) \leq 0$, the satellite is generally moving toward the Sun, so the area-to-mass ratio is set to its maximum value, indicating a fully inflated balloon. Conversely, when $cos(\theta) > 0$, the balloon is set to be fully deflated, and the area-to-mass ratio switches to its minimum value.

As mentioned in Section 2.3.1, the ratio values used in this study were 0.04 $m^2/kg$ and 1.0 $m^2/kg$. The area-to-mass ratio values over time for a balloon experiencing binary inflation and deflation over 36 hours are shown in Figure 4.2, while the cosine values for this balloon are displayed in Figure 4.3.

As shown in Figures 4.2 and 4.3, the balloon's area-to-mass ratio automatically switches between its minimum and maximum values as the sign of the line of the cosine values

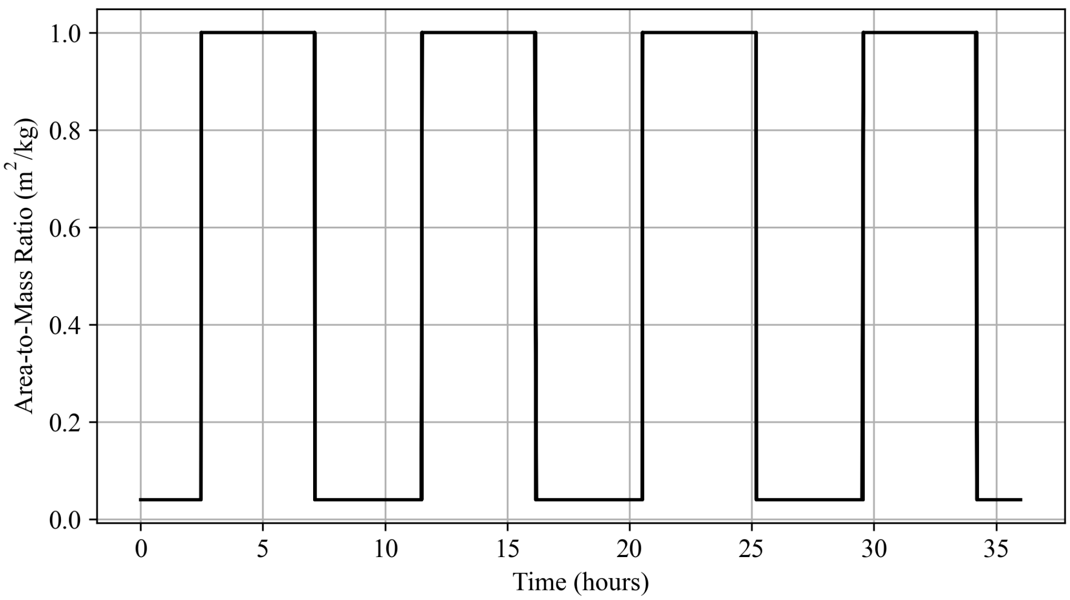


FIGURE 4.2: Area-to-mass ratio in $m^2/kg$ for a balloon deploying binary inflation and deflation over 36 hours.

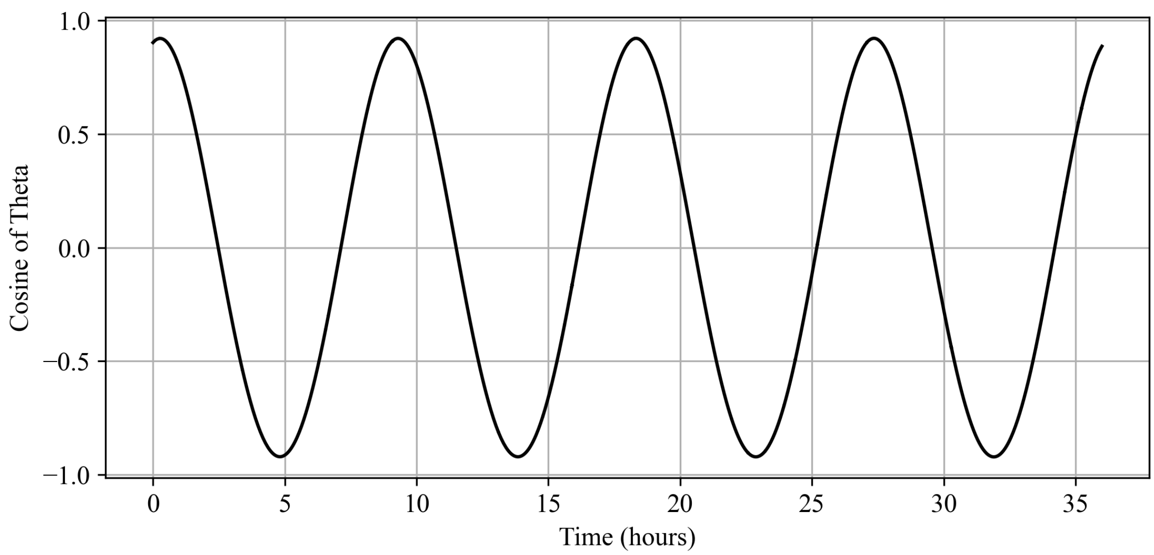


FIGURE 4.3: Cosine of theta values for a balloon deploying binary inflation and deflation over 36 hours.

crosses the x-axis, indicating a shift in direction of the balloon with respect to the SRP vector. Furthermore, the times when the balloon is deflated correspond with positive cosine values, while the times when the balloon is inflated line up with negative cosine values.

The change in the semi-major axis values over this 36-hour period for the satellite deploying a binary inflation and deflation process compared to that of a fully deflated balloon is shown in Figure 4.4.

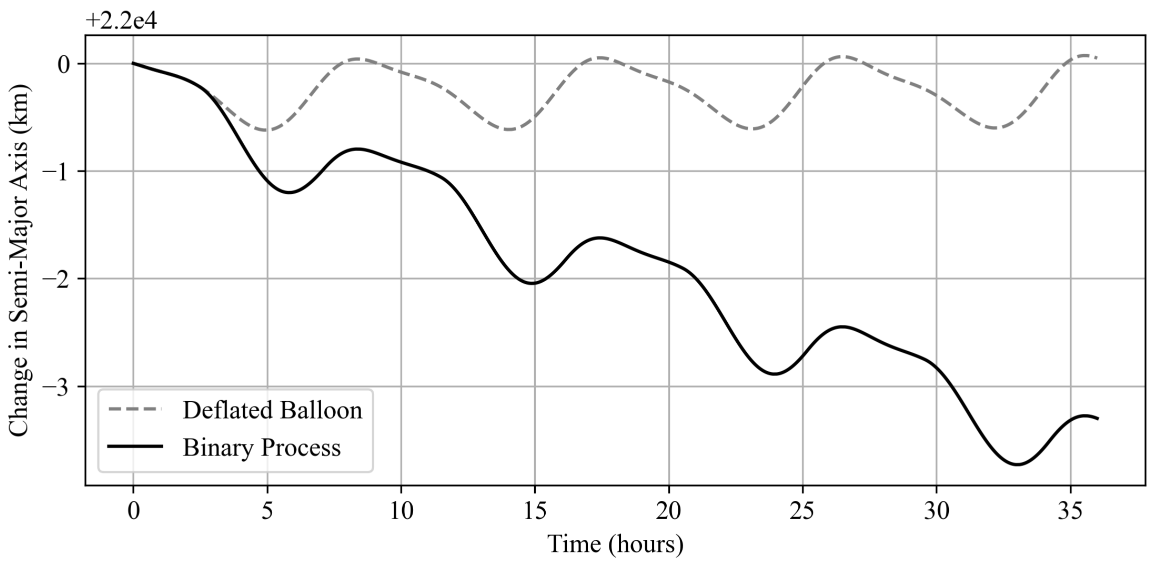


FIGURE 4.4: Comparison of the change in the semi-major axis in km over 36 hours for a balloon using binary inflation and deflation and a fully deflated balloon.

The semi-major axis values for the balloon using binary inflation and deflation show a significant deviation in behavior from those modeled using a fully deflated balloon, which is pulled from the same data set used in Figure 2.5. The effect of the inflated balloon is clearly visible, as the semi-major axis experiences a significant decrease during deployment, while the periods correlated to a deflated balloon match the baseline behavior observed in Figure 2.5. These alterations to the natural deviations of the semi-major axis indicate that the model for deploying the balloon is working correctly.

### 4.2.1 Inclination Trends

As previously discussed in Section 2.3.2, inclinations of 0.001, 23.44, 56.06, and 90 degrees were considered for balloon tests. The calculated values for the cosine over 10 years at each of these inclinations for a fully deflated balloon with a reflectivity coefficient of 1.88 are shown in Figure 4.5. As the inflation and deflation model relies on the identification

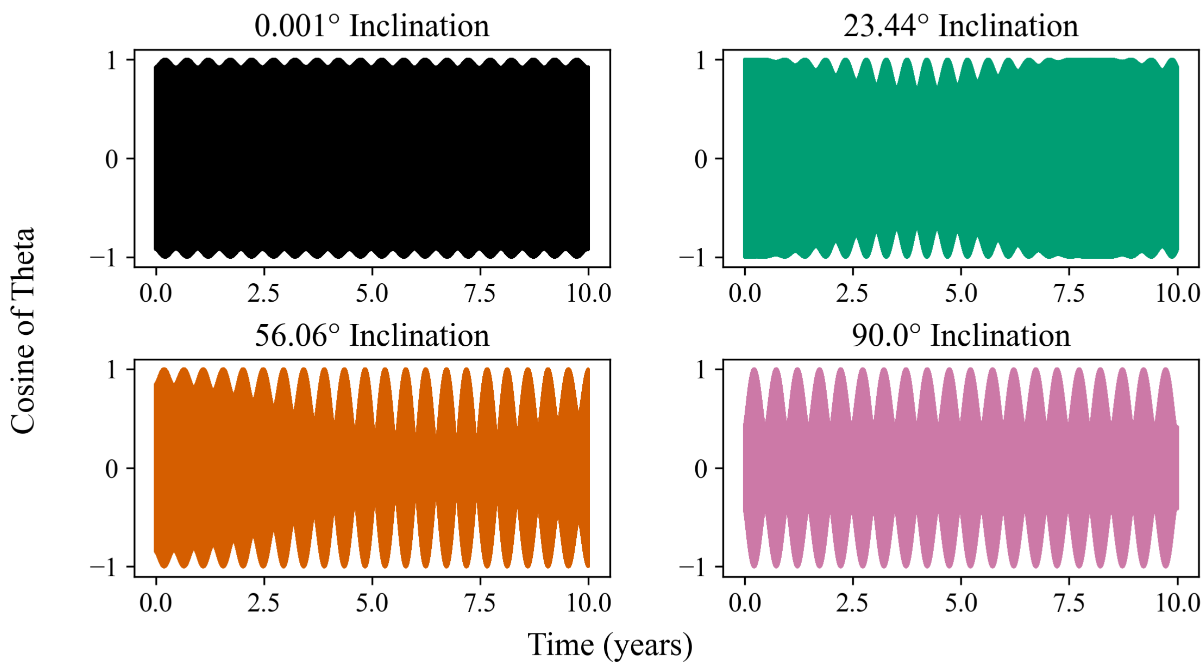


FIGURE 4.5: Cosine of theta over 10 years for a fully deflated balloon with initial inclination values of 0.001 (top left), 23.44 (top right), 56.06 (bottom left), and 90.0 degrees (bottom right).

of the cosine around values of 0, the graphs in Figure 4.5 offer promising results. For all inclinations tested, the region along the x-axis where the sign change of the cosine occurs displays a uniform behavior with no unexpected gaps in the data.

Conversely, there is a clear difference in the range of calculated cosine values over time between each of the initial inclinations. The initial 0.001-degree inclination produced the most uniform results, with a minimal sinusoidal change in the maximum and minimum cosine values. For the 90.0-degree inclination trial, there is a similarly homogeneous sinusoidal trend with a nearly identical wavelength. However, the amplitude of the troughs is much lower than that in the 0.001-degree trial, which could be an indication that the polar orbit periodically shifts so that the satellite is traveling nearly perpendicular to the SRP, yielding less acceleration due to the perturbation.

The 23.44 and 56.06-degree trials introduce longer periodic sinusoidal trends on top of the shorter sinusoidal waves. Interestingly, the 23.44-degree trial experienced times where the amplitude of these waves remained close to 1, including from the start of the trial until about 0.6 years, and again between around 7.5 and 8.75 years. These periods of time are likely when the orbit is nearly parallel to the ecliptic plane before its inclination begins to deviate. The large, sinusoidal decrease in the trough amplitude of the 56.06-degree graph may be attributed to the resonance associated with that inclination.

### 4.2.2 Reflectivity

To better explore the relationship between the solar sail's material properties and the balloon's orbital behavior, the model was used to track the effect of various reflectivity coefficient values on the semi-major axis for binary inflation and deflation. Trials were conducted using an initial near-equatorial inclination of 0.001 degrees, a 5-year time frame, and an initial semi-major axis of 22,000 km. The coefficient values started at 1.0 and increased in increments of 0.1 until the maximum possible reflectivity coefficient of 2.0 was reached, as shown in Figure 4.6.

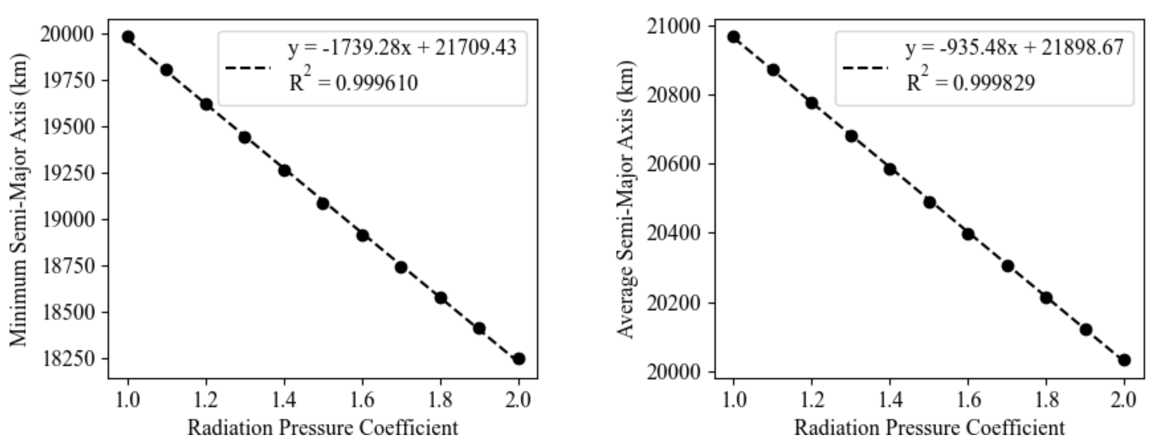


FIGURE 4.6: Minimum (left) and average (right) semi-major axis values after 5 years for a balloon deploying binary inflation and deflation.

According to Figure 4.6, there is a linear correlation between the reflectivity coefficient and both the minimum and average semi-major axis values after one year. As the reflectivity coefficient of the material increases, the force due to SRP proportionally increases, explaining the lower minimum and average semi-major axis values for the higher coefficient trials. Thus, in an ideal scenario, the balloon should have the highest reflectivity value possible to maximize the effect of SRP, a relationship indicated in Equation 2.11.

It should also be noted that a binary inflation and deflation trial with the same parameters as the reflectivity tests and a coefficient of 1.88 yielded a minimum semi-major axis of 18445.2462 km and an average of 20141.9789 km, which are extremely close to their respective values of 18439.5836 km and 20139.9676 km predicted by the linear trend line equations in Figure 4.6. The deviation in these values from the predicted number can be explained by the value of $R^2$ for each trend line, as they are nearly, but not perfectly, linear.

Thus, these relations can be used to estimate the minimum and average semi-major axis values for any reflectivity coefficient with the same test parameters. It is also important to recall that the chosen reflectivity value is assumed constant across the entire apparent area of the satellite, as the device is assumed to be a uniform sphere for the cannonball model calculations from Chapter 2.

### 4.2.3 Binary Process Re-Entry Results

When identifying the best-case initial conditions for the simulation, all four trial inclinations were first tested over a 50-year period to track their long-term behavior using binary inflation and deflation. This time limit was put in place due to the extended period of time required to run each test. The resulting plots of the semi-major axis and eccentricity values over time are shown in Figures 4.7 and 4.8.

As shown in Figure 4.7, the satellite was able to complete the re-entry process using binary inflation and deflation in about 35.72 years when starting with a 0.001-degree inclination and about 42.86 years when orbiting with an initial inclination of 23.44 degrees. While the satellite in the 56.06-degree orbit managed to reach the outer limits of the atmosphere, as shown by the quick decrease in its semi-major axis at the end of the plot, it was unable to complete the de-orbiting process with the 50-year time frame, though it is

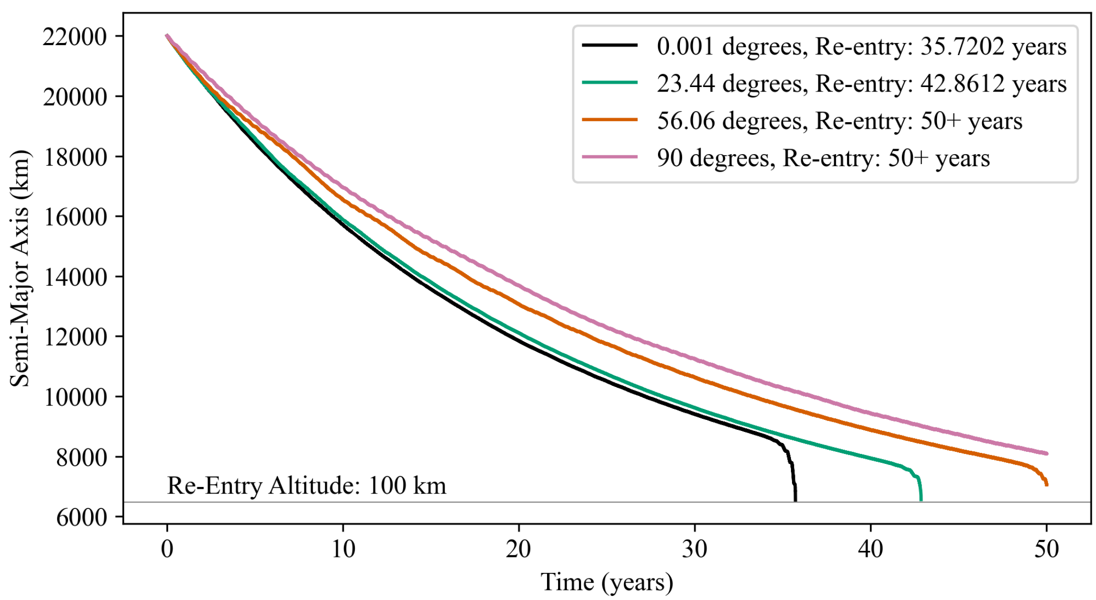


FIGURE 4.7: Semi-major axis values in km over 50 years (or until atmospheric re-entry) for a satellite deploying the balloon with binary inflation and deflation at inclinations of 0.001, 23.44, 56.06, and 90 degrees.

likely that total re-entry would occur between 50 and 52 years based on the trends of the two successful trial curves. The satellite in the polar orbit was unable to breach the upper limits of the atmosphere during this test.

Regardless of inclination, the overall trends for the semi-major axis values displayed in Figure 4.7 are very similar. If the first 5 years of these orbits were to be plotted, they would display a decrease in their semi-major axis values that appears remarkably linear. However, as this value continues to decrease, the slope of these curves starts to flatten out, meaning that the orbit is shrinking at a slower rate than before, and the spherical sail becomes less efficient. This is likely due to a combination of two reasons.

First, while the satellite orbits at higher altitudes, the perturbations due to SRP are dominant in the system, making the de-orbiting process extremely efficient. As the satellite gets closer to the Earth, however, the perturbations due to the planet's oblateness and gravity begin to limit the prominence of the acceleration due to SRP in the satellite's EOM.

The second reason is that as the balloon gets closer to the Earth, the size of the planet's shadow gets larger and larger, resulting in less exposure to sunlight and, consequently, radiation pressure with every period. The sharp decline in the semi-major axis at the end of these trials is a clear sign that the satellite has encountered severe drag from the atmosphere. The trends in eccentricity for these 50-year trials, as shown in Figure 4.8, are less uniform. First, the sharp increase in eccentricity shown in the 0.001 and 23.44-degree tests is a clear sign that the satellite encountered a resonance of some kind. It is beyond the scope of this analysis to determine the cause of these resonances, as they can arise from numerous combinations of orbital elements and perturbations. However, a connection between these rising eccentricities and the faster re-entry times can be drawn.

Similarly, the slower re-entry process of the polar orbit can be tied to the surprising drop in its eccentricity after about 30 years, which is likely also due to a resonance of some kind. Another reason behind this slow progress to a lower orbit could be due to the periodic trend of the satellite to fly nearly perpendicular to the SRP vector, as shown in Figure 4.5 and previously discussed. Regarding the 56.06-degree trial, the steady rise in eccentricity aligns with the expected behavior of orbits at this inclination for this time frame, as was discussed in Section 2.3.2. This test also exhibited a near-instant drop in eccentricity at the point where the satellite made contact with the atmosphere, which can also be observed in the 0.001 and 23.44-degree plots. This sudden shift back to a more

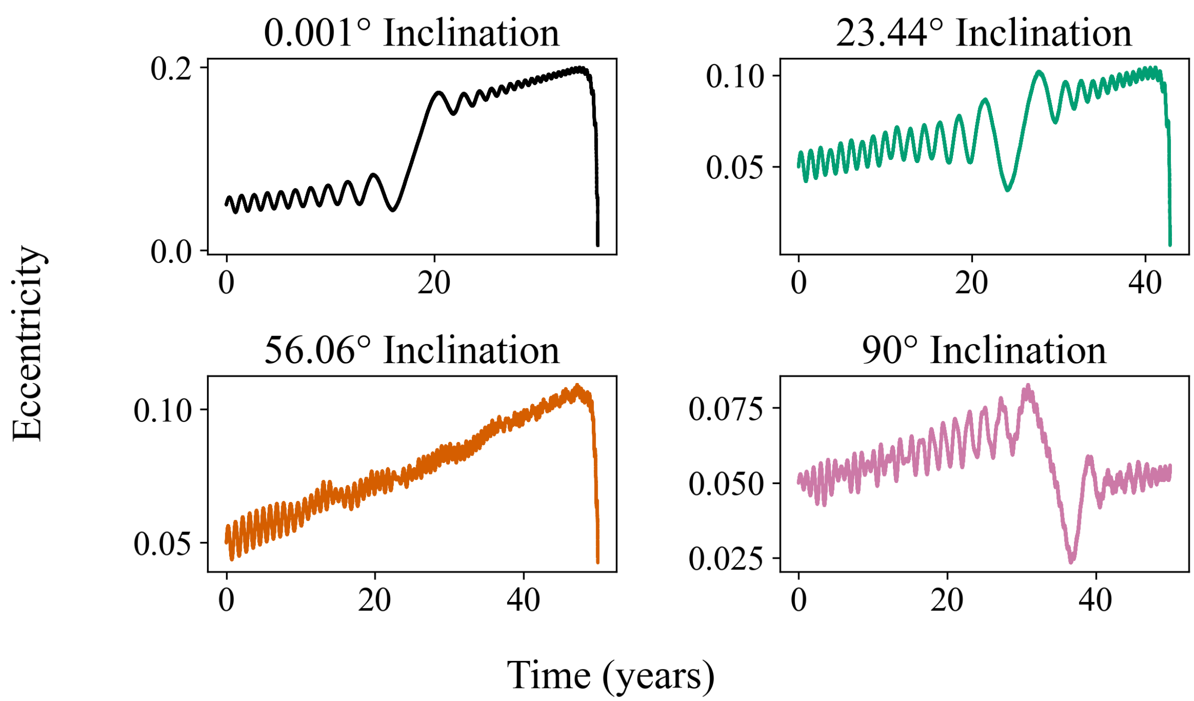


FIGURE 4.8: Eccentricity over 50 years (or until atmospheric re-entry) for a satellite deploying the balloon with binary inflation and deflation at inclinations of 0.001 (top left), 23.44 (top right), 56.06 (bottom left), and 90 degrees (bottom right).

circular orbit is due to the rapidity with which the satellite's velocity decreases under the influence of atmospheric drag.

## 4.3 Linear Inflation and Deflation

Contrary to the process of binary inflation and deflation, where the model determines the satellite's area-to-mass ratio based only on the current sign of the cosine value, linear changes to the balloon's size are activated by a flip in the sign. To be more specific, the model is programmed to recognize when the satellite velocity changes direction with respect to the SRP vector by comparing each cosine of theta value with the value from the previous iteration. If the product of these two numbers is negative, the satellite has changed direction. While the possibility for the cosine of theta to equal 0 has been included in the logic, it should be noted that this is an extremely rare occurrence due to the precise nature of the integrator calculations. For simplicity, it was decided to associate cosine values of 0 with negative cosine values. The logic behind this process is visually represented in Figure 4.9.

As shown in Figure 4.9, the current and former values of the cosine, $cos(\theta_i)$ and $cos(\theta_{i-1})$, are the primary drivers behind the model's decision to inflate or deflate the balloon. If the product between these two values is greater than 0, the satellite is assumed to be traveling in the same direction as it was before, and will continue either inflating or deflating the balloon until it reaches its target area-to-mass ratio.

### 4.3.1 Linear Inflation Process

If the product between them is less than or equal to 0, the satellite's velocity has changed direction with respect to the SRP vector. If the former cosine value is greater than 0, meaning the device was previously traveling with the SRP, and will now be flying against it, the linear inflation process is activated. First, the instantaneous period of the orbit, $T_{inst}$, is calculated using:

$$T_{inst} = 2\pi\sqrt{\frac{a^3}{\mu_\oplus}} \tag{4.2}$$

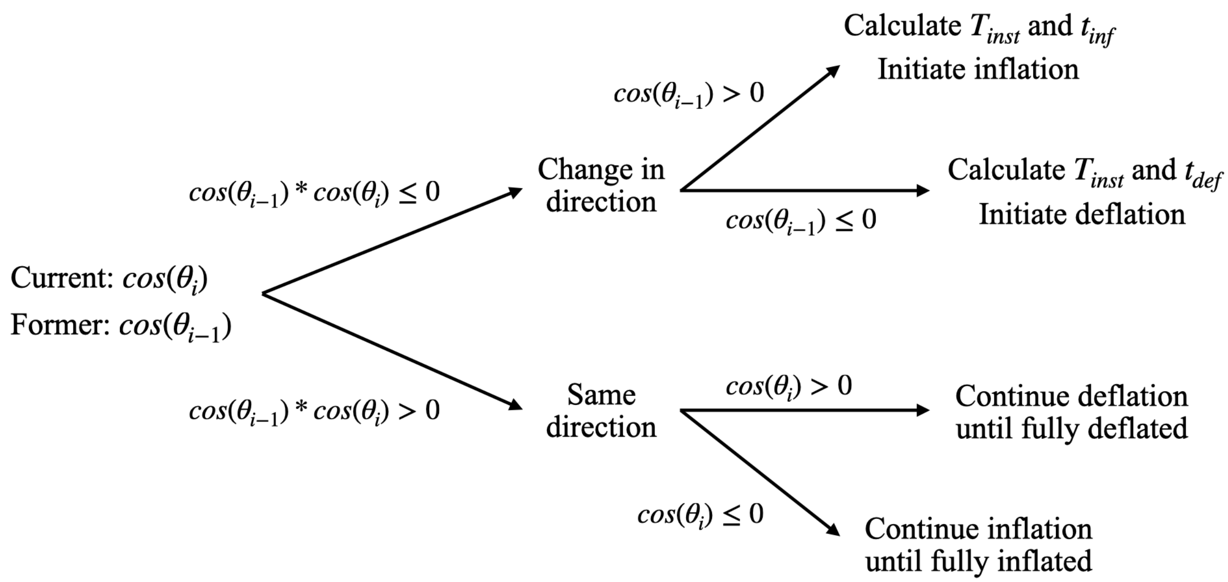


FIGURE 4.9: Logic of linear inflation and deflation depending on the current and former values of the cosine of theta.

where a is the semi-major axis at the time the calculation is performed. The total time for inflation, $t_{inf}$, is then calculated by adding the time inflation was initiated, $t_{inf,0}$, to a fraction of the period:

$$t_{inf} = t_{inf,0} + \frac{T_{inst}}{N_{inf}} \tag{4.3}$$

where $N_{inf}$ is defined by the user. In essence, once the time $t_{inf}$ has been reached, the balloon will be fully inflated. This process is conducted using $n$ number of time steps between $t_{inf,0}$ and $t_{inf}$ as signals to inflate the balloon to a certain area-to-mass ratio for each step. A visual representation of this inflation process compared to an ideal process is shown in Figure 4.10.

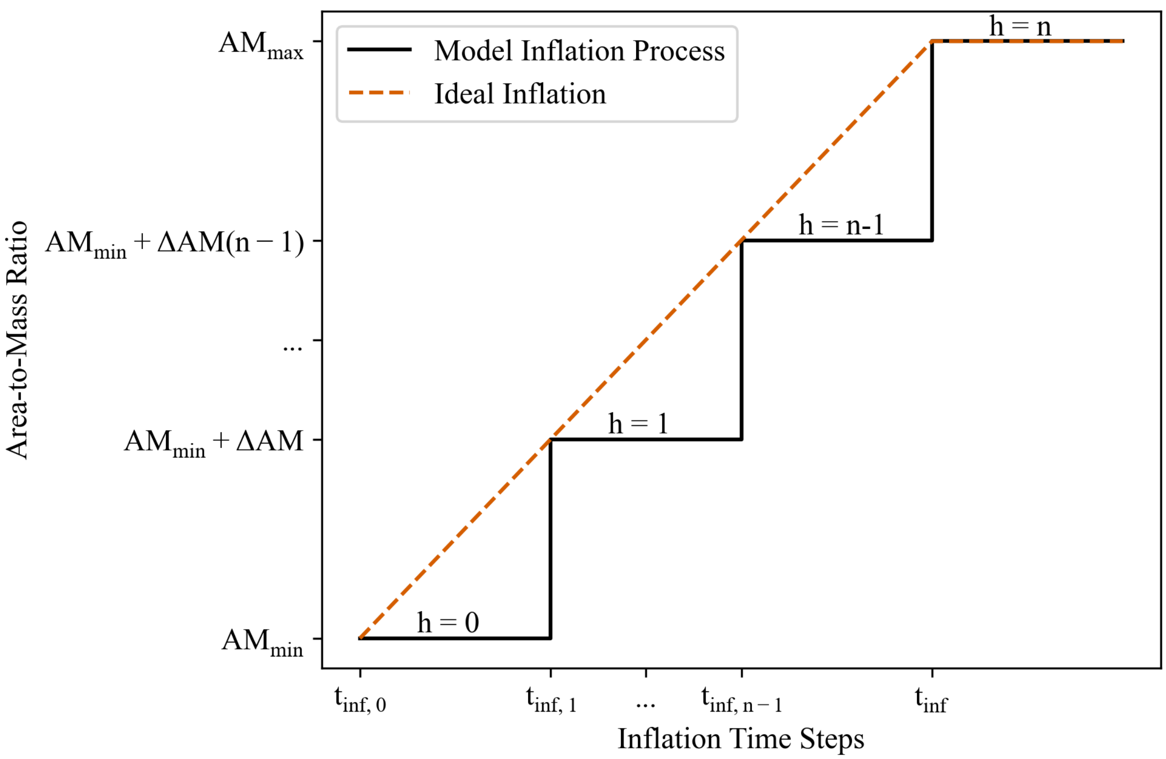


FIGURE 4.10: Ideal and modeled linear inflation process of the area-to-mass ratio for $n$ time steps.

The area-to-mass ratio value at each step in the inflation process is calculated using:

$$AM = AM_{min} + (h\Delta AM) \tag{4.4}$$

where $h$ is a number that indicates the current step, the change in the area-to-mass ratio $\Delta AM$ is found by dividing the difference between the maximum and minimum ratio values, $AM_{max}$ and $AM_{min}$, by the number of steps, $n$:

$$\Delta AM = \frac{AM_{max} - AM_{min}}{n} \tag{4.5}$$

and $h$ is a value that ranges from 0 to $n$ depending on the current time step. To maintain conservatism in the model, the area-to-mass ratio will not increase by $\Delta AM$ until after a new time step is reached. For example, when the current time $t$ falls between $t_{inf,0} \leq t < t_{inf,1}$, the value of $h$ will be set to 0, and the area-to-mass ratio will be calculated as the minimum value, $AM_{min}$, using Equation 4.4. Similarly, when the time $t$ is between $t_{inf,n-1} \leq t < t_{inf}$, $h$ will take the value of $n-1$, and the area-to-mass ratio will be calculated accordingly. For any time $t \geq t_{inf}$ while the cosine remains less than or equal to 0, the area-to-mass ratio will be set equal to its maximum value until a direction change is detected and the deflation process begins.

### 4.3.2 Linear Deflation Process

To reiterate, if the product between them is less than or equal to 0, the satellite's velocity has changed direction with respect to the SRP vector. If the former cosine value is less than or equal to 0, meaning the device was previously traveling against the SRP and will now be flying with it, the linear deflation process is activated. First, the instantaneous period of the orbit, $T_{inst}$, is calculated using Equation 4.2. Next, the total time for deflation, $t_{def}$, is then calculated by adding the time deflation was initiated, $t_{def,0}$, to a fraction of the period:

$$t_{def} = t_{def,0} + \frac{T_{inst}}{N_{def}} \tag{4.6}$$

where, similarly to the inflation process, $N_{def}$ is defined by the user, and the balloon will be fully deflated once the time $t_{def}$ has been reached. Similarly to the inflation process, there are $n$ time steps between $t_{def,0}$ and $t_{def}$ that indicate the correct area-to-mass ratio. A visual representation of the deflation process is shown in Figure 4.11.

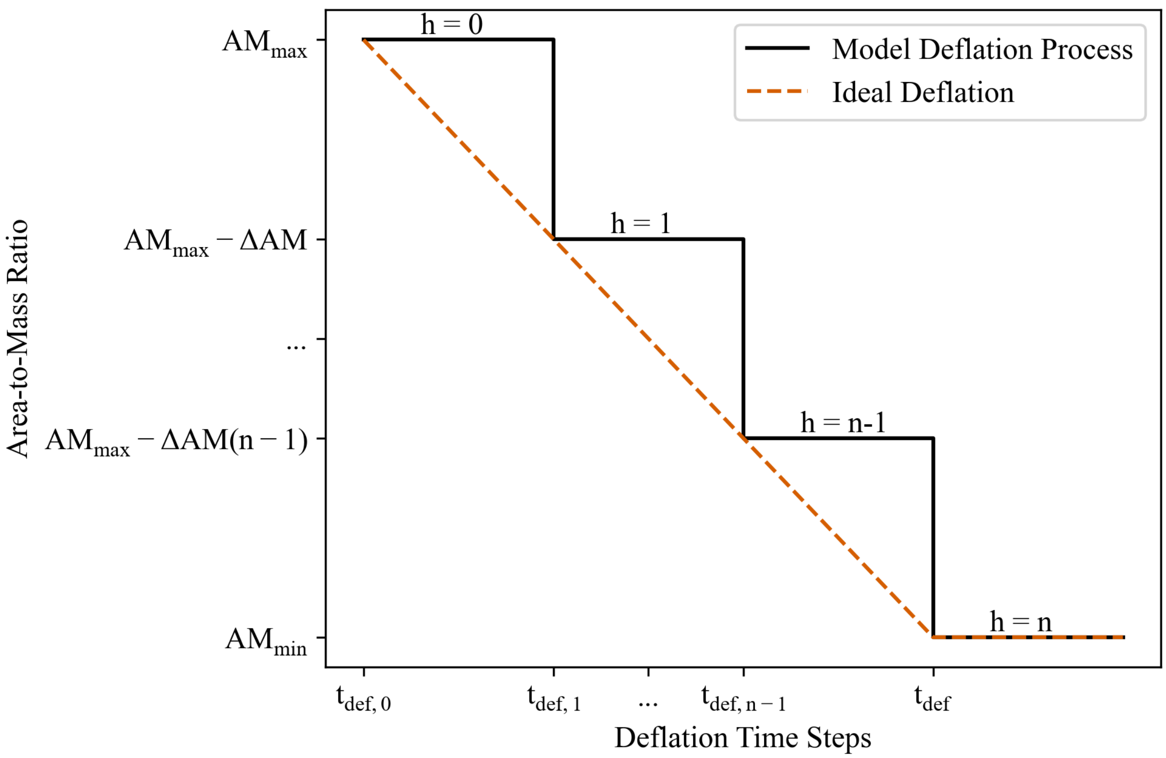


FIGURE 4.11: Ideal and modeled linear deflation process of the area-to-mass ratio for $n$ time steps.

The area-to-mass ratio value at each step in the deflation process is calculated using:

$$AM = AM_{max} - (h\Delta AM) \tag{4.7}$$

where $h$ is a number that indicates the current step, the change in the area-to-mass ratio $\Delta AM$ is found using Equation 4.5, and the value of $h$ ranges from 0 to $n$, and correlates with each time step, as shown in Figure 4.11. Just as with inflation, a level of conservatism was implemented into the linear deflation process, as the area-to-mass ratio will not decrease by $\Delta AM$ until a new time step is reached.

For example, when the current time $t$ falls between $t_{def,0} \leq t < t_{def,1}$, the value of $h$ will be 0, and the area-to-mass ratio will be calculated as the maximum value, $AM_{max}$, using Equation 4.7. Furthermore, when the time $t$ is between $t_{def,n-1} \leq t < t_{def}$, $h$ will be set to $n-1$, and the area-to-mass ratio will be calculated accordingly. For any time $t \geq t_{def}$ while the cosine remains greater than 0, the area-to-mass ratio will be set equal to its minimum value until a direction change is detected and the inflation process begins.

It is important to note that in an effort to maintain linear behavior regardless of the length of the period or selected inflation and deflation rates, the number of steps, $n$, was set to 1000 for all trials using linear processes.

A visual demonstration of the linear inflation and deflation processes is shown in Figure 4.12, where the satellite is in a counter-clockwise orbit. A visual comparison between the various inflation and deflation methods is shown in Figure 4.13.

The minimum area-to-mass ratio, which is the only value for the fully deflated balloon in the top left graph of Figure 4.13, is set to 0.04 m$^2$/kg, while the maximum value is 1.0 m$^2$/kg, as it is for all trials. For visual clarity on the linear processes, the period fraction values of $N_{inf}$ and $N_{def}$ from Equations 4.3 and 4.6 are both set to 16.

### 4.3.3 Linear Inflation and Binary Deflation Behavior

The behavior of the balloon for various inflation times was tested by allowing inflation to occur over increasing percentages of the total period. For each trial, the initial conditions included a semi-major axis of 22,000 km, an inclination of 0.001 degrees, an eccentricity of 0.05, a reflectivity coefficient of 1.88, and a test length of 1 year. The results of these trials are shown in Figure 4.14.

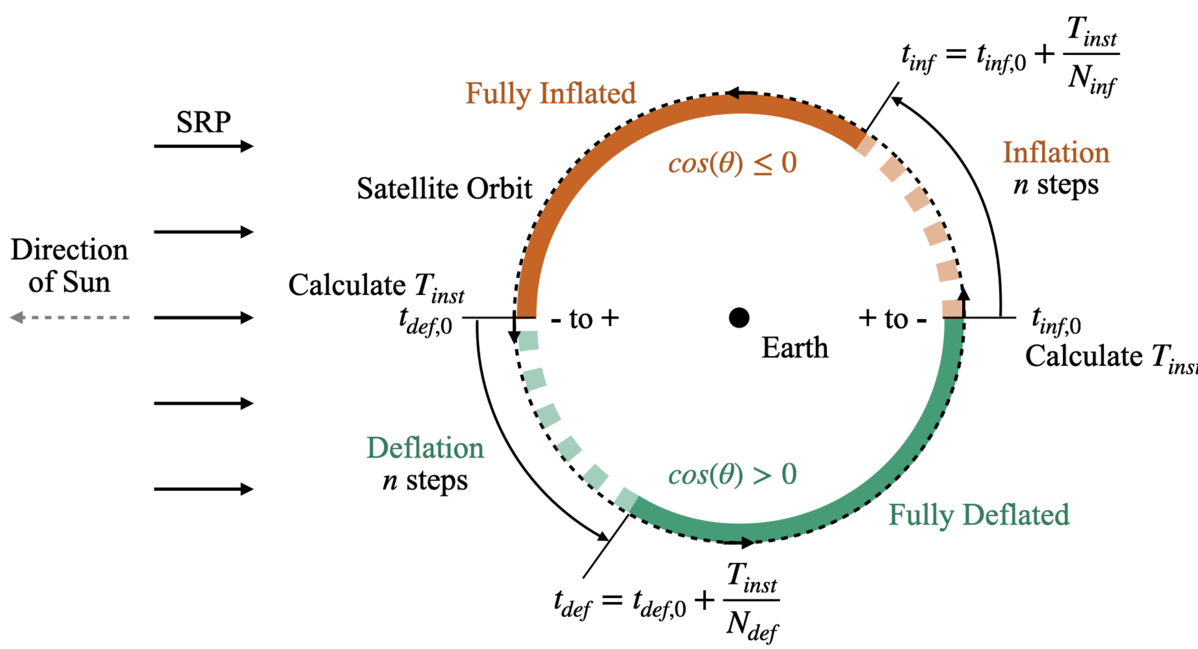


FIGURE 4.12: Visual demonstration of the linear inflation and deflation processes.

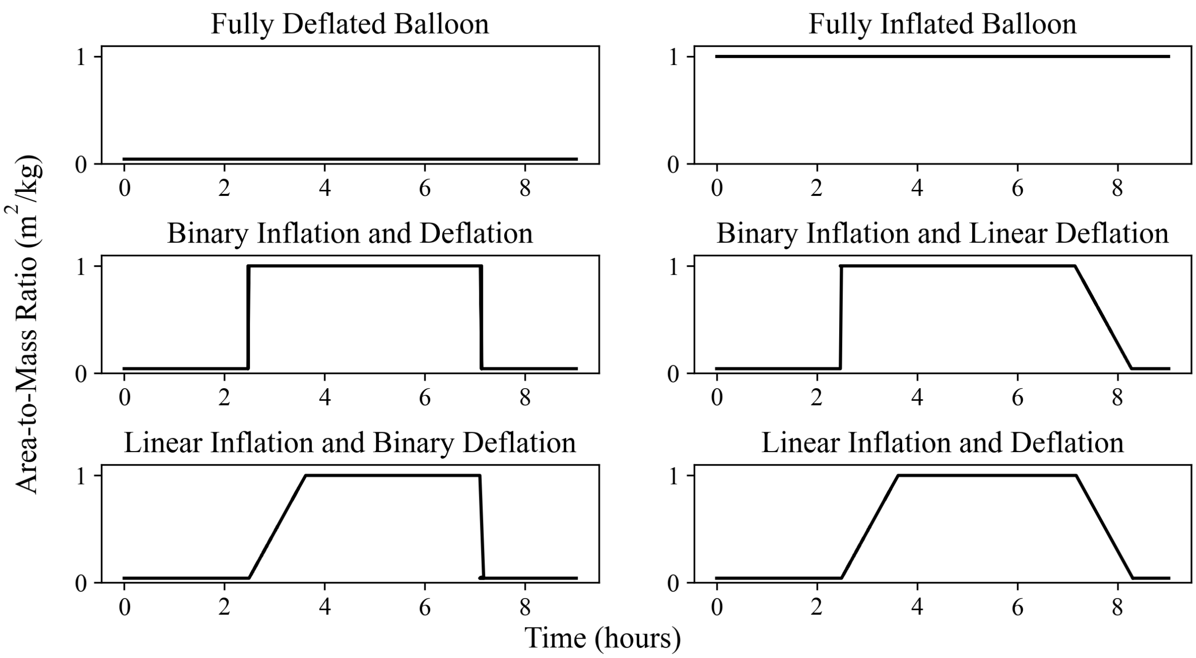


FIGURE 4.13: Area-to-mass ratio over one period for a fully inflated and deflated balloon, as well as combinations of binary and linear inflation and deflation methods.

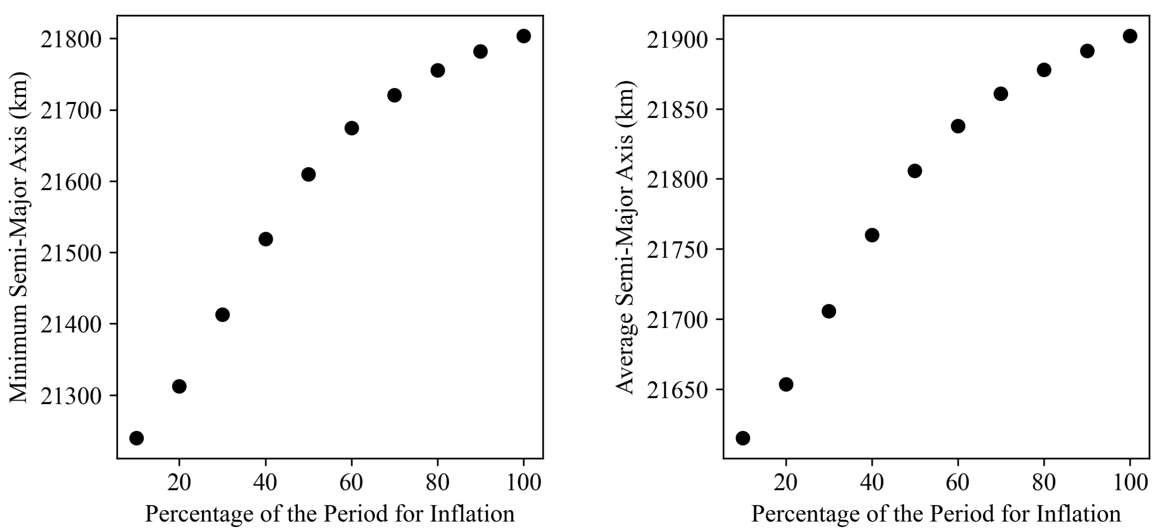


FIGURE 4.14: Minimum (left) and maximum (right) semi-major axis values in km after 1 year for linear inflation over percentage intervals of the instantaneous period and binary deflation.

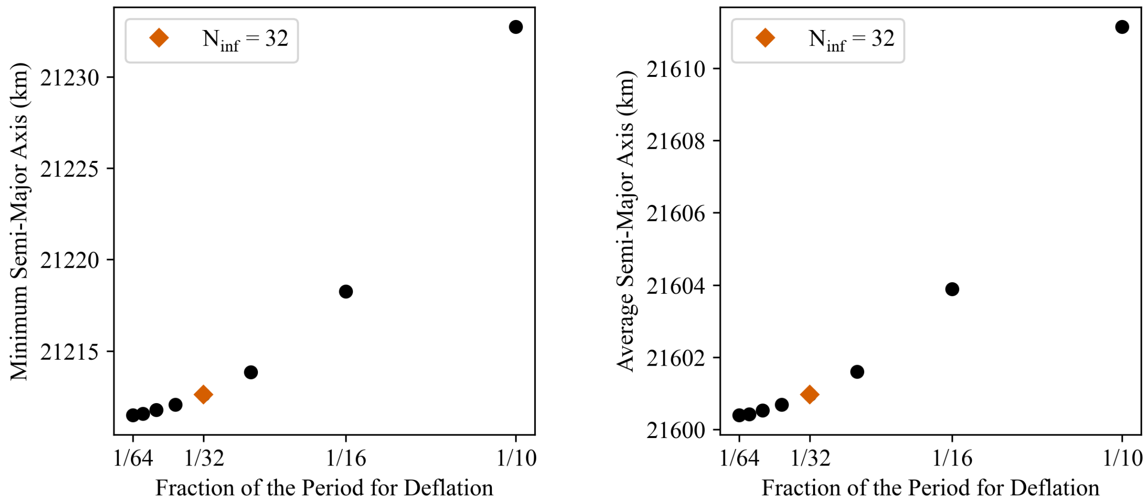


FIGURE 4.15: Minimum (left) and average (right) semi-major axis values in km after 1 year for linear inflation over small fractions of the period and binary deflation.

As displayed in Figure 4.14, between the 20 percent and 50 percent intervals, the trend is nearly linear, with the increase in efficiency dropping off with longer inflation periods after that. The most efficient inflation method in terms of lowering the semi-major axis values was the 10 percent interval, as the balloon was fully inflated for a majority of its time traveling against the SRP.

To identify a realistic fraction of the period for linear inflation to occur, the model was next used to run trials with linear inflation and binary deflation over various fractions of the instantaneous period, $T_{inst}$, as seen in Equation 4.3. The binary process was hypothesized to be the most efficient method, as the semi-major axis values were lower for the shorter inflation times. Thus, an emphasis was placed on testing linear inflation over smaller, yet feasible, fractions of the period. The inflation times were calculated using Equation 4.3 with the following $N_{inf}$ values: 16, 24, 32, 40, 48, 56, and 64. The minimum and average semi-major axis values from each trial were then plotted against the fraction of the period over which the linear inflation occurred, as shown in Figure 4.15.

As predicted, limiting the required inflation time of the balloon yields better results in terms of decreasing the semi-major axis. The lowest values for both the minimum and average semi-major axis result from the trial with the shortest inflation time of one sixty-fourth of the period. The fact that the average values display the same trend as the minimum values is an indication that the individual plots of the semi-major axis will follow the same general structure as the binary process in Figure 4.7, only with steeper slopes for shorter inflation times.

The best-case value of $N_{inf}$ was chosen to be 32 for three reasons. First, the differences between the results when $N_{inf}$ is 24, 32, and 64 are minimal, as they are at the base of what appears to be an exponential trend. Second, there is a decrease in the computation time for lower values of $N_{inf}$, as the model completes the calculations for the inflation process across fewer time steps. Finally, when considering real-world applications of this system, less time for inflation means the gas must be pumped into the balloon faster, which will likely generate more heat within the compressor due to the increased mass flow rate. Considering that an $N_{inf}$ value of 24 results in longer computation times and a value of 64 provides minimal benefits while doubling the required mass flow rate of the compressor, the decision to use 32 for $N_{inf}$ is reasonable.

### 4.3.4 Binary Inflation and Linear Deflation Behavior

The behavior of the balloon was next tested for various deflation times by allowing the deflation process to occur over increasing percentages of the total period. The model was set with identical initial conditions as those used in the linear inflation and binary deflation tests. The results of these trials are shown in Figure 4.16.

Figure 4.16 shows a similar trend to that of Figure 4.14, in that the shorter processing time for the balloon to change sizes will result in more ideal values for the semi-major axis. There is also a similar plateau in the efficiency, with minimal changes to the resulting values.

As done with the inflation trials, the model was next used to run trials with binary inflation and linear deflation over various fractions of the instantaneous period, $T_{inst}$, as seen in Equation 4.6, to identify an ideal deflation period. The deflation times were calculated using Equation 4.6, with the following $N_{def}$ values: 16, 24, 32, 40, 48, 56, and 64. The minimum and average semi-major axis values from each trial were then plotted against the fraction of the period in which the linear deflation occurred, as shown in Figure 4.17.

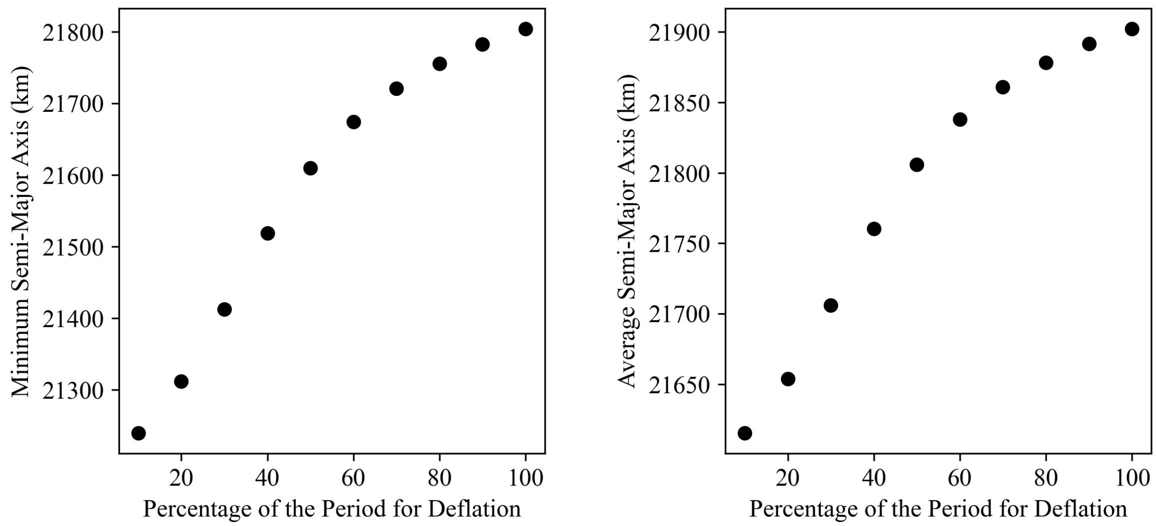


FIGURE 4.16: Minimum (left) and maximum (right) semi-major axis values in km after 1 year for binary inflation and linear deflation over percentage intervals of the instantaneous period.

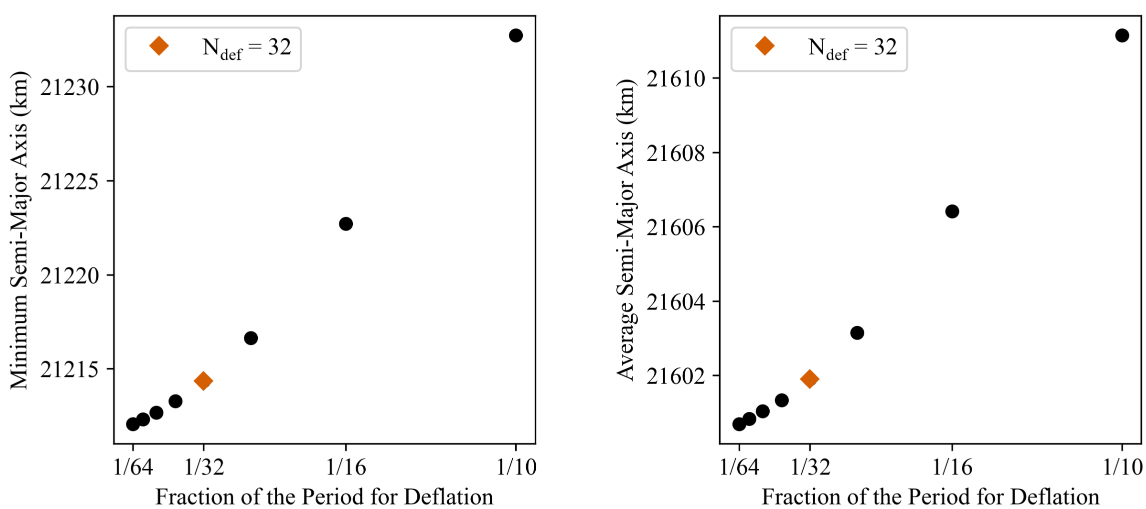


FIGURE 4.17: Minimum (left) and average (right) semi-major axis values in km after 1 year for binary inflation and linear deflation over small fractions of the period.

It is abundantly clear from Figure 4.17 that longer deflation periods will yield higher minimum and average semi-major axis values. Due to the high similarity between the results of the linear inflation and deflation tests, a final value of 32 for $N_{def}$ was selected, and the reasoning behind this choice remains the same as it was for the linear inflation trials.

## 4.4 Long-Term Comparison of Methods

To truly understand the magnitude of the effect this de-orbiting method has on the satellite's trajectory, the semi-major axis values for a fully deflated balloon and a satellite using linear inflation and deflation to harness SRP over 10 years at an inclination of 0.001 degrees were compared in Figure 4.18.

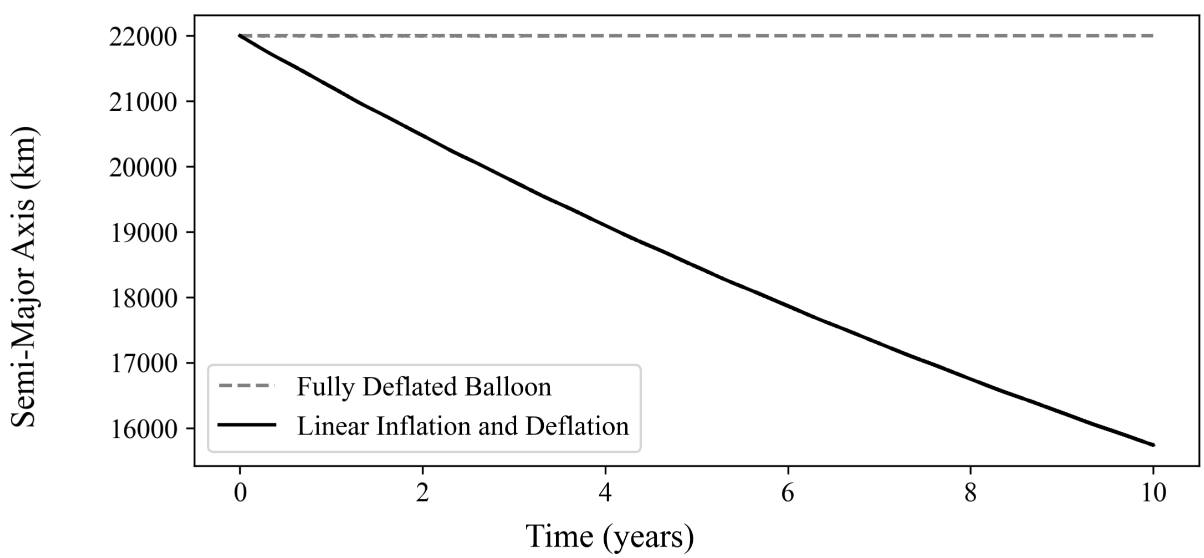


FIGURE 4.18: Comparison of the semi-major axis over 10 years for a fully deflated balloon and a satellite using linear inflation and deflation.

The difference between deploying the balloon using linear inflation and leaving the presumed non-functional satellite is extremely apparent in Figure 4.18. The model demonstrates how the balloon is capable of decreasing the semi-major axis of the orbit by over 6000 km in just 10 years. When plotting the 10-year binary and linear processes, the two lines are nearly indiscernible from one another. For clarity, the semi-major axis values from only the last year of these trials are compared in Figure 4.19.

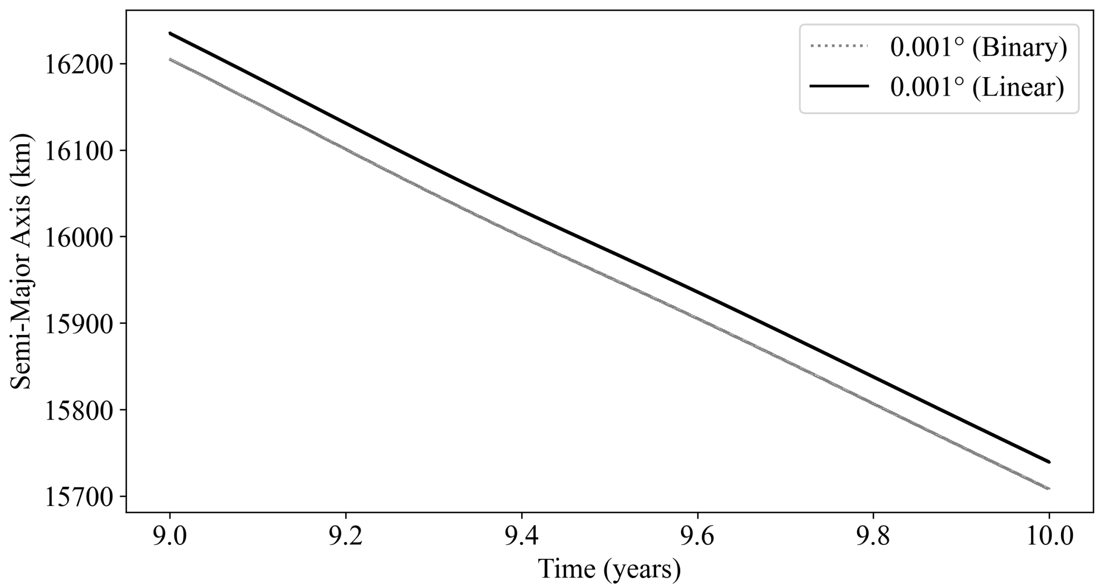


FIGURE 4.19: Comparison of semi-major axis values for the binary and linear processes for the last year of a 10-year trial.

Figure 4.19 shows that while binary inflation and deflation are the ideal processes for harnessing the SRP to de-orbit, the linear process is extremely efficient, with a mere 31.22 km difference in their final semi-major axis values after 10 years.

# Chapter 5

# Real-World Applications

## 5.1 Best-Case Solutions

In order to determine the best-case solution for the proposed de-orbiting model, it is first important to reiterate the constraints that each trial adhered to. First, the initial semi-major axis value was 22,000 km, and a near-circular initial eccentricity of 0.05 was employed. The chosen reflectivity coefficient value was 1.88, and the initial values for the argument of the perigee, right ascension of the ascending node, and mean anomaly were set to 0 degrees. The area-to-mass ratio of the 100 kg satellite ranged from 0.04 to 1.0 $m^2$/kg, and both $N_{inf}$ and $N_{def}$ were set to 32 per the reasoning in Section 4.3.3, meaning that the inflation and deflation processes occurred over one-thirty-second of the period.

In terms of the ideal set-up to attain the minimum time until re-entry, it is appropriate to model the 0.001-degree orbit using linear inflation and deflation as a baseline, as this inclination yielded the fastest re-entry time during the binary trials in Section 4.2.3. Furthermore, as this study is meant to model the de-orbit process for non-functional satellites in graveyard GNSS orbits, the linear process for a 56.06-degree inclination orbit is also plotted in Figure 5.1. As shown in Figure 5.1, the time until atmospheric re-entry for a satellite with an initial inclination of 0.001 degrees is approximately 34.9608 years, which is surprisingly 0.7594 years (or 9.1128 months) faster than the binary process with the same initial parameters shown in Figure 4.7. The 56.06-degree trial resulted in a re-entry time of 50.1407 years. The eccentricity values for these trials are shown in Figure 5.2.

The decrease in the total time for the 0.001-degree de-orbit process could be due to the conditions present when the satellite began to experience resonance. For example, the slight deviations in eccentricity, inclination, semi-major axis, or any other orbital element

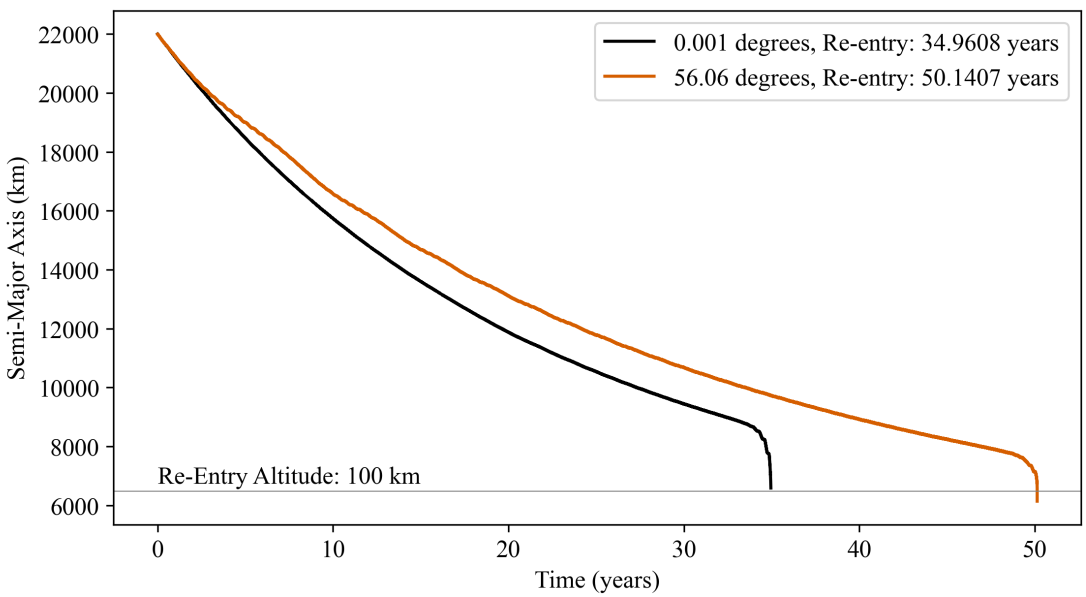


FIGURE 5.1: Semi-major axis values in km over time in years until atmospheric re-entry for a satellite deploying the balloon with linear inflation and deflation at inclinations of 0.001 and 56.06 degrees.

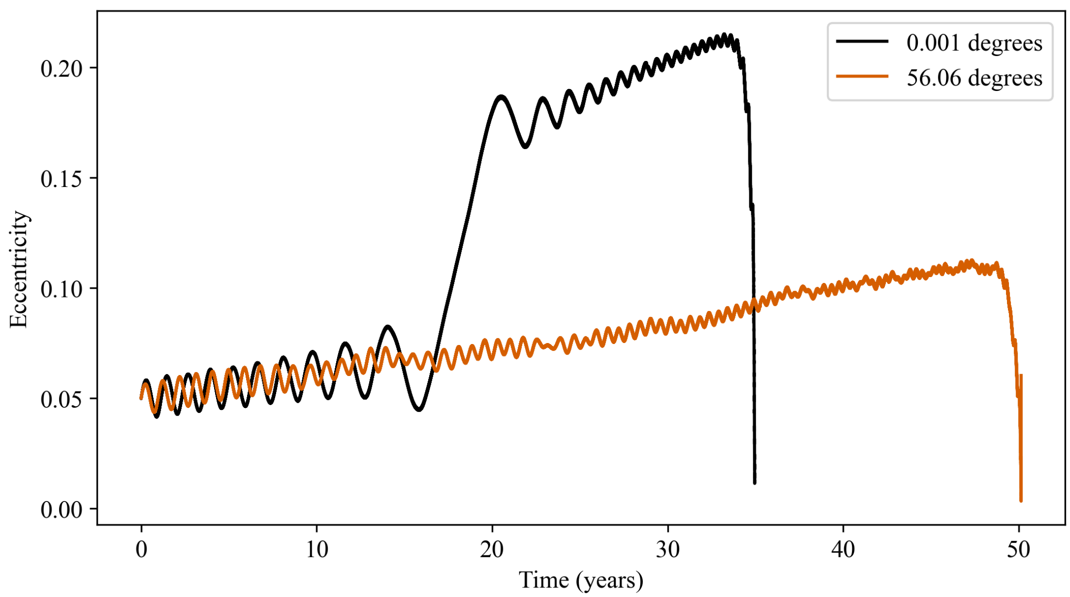


FIGURE 5.2: Eccentricity over time in years until atmospheric re-entry for a satellite deploying the balloon with linear inflation and deflation at inclinations of 0.001 and 56.06 degrees.

due to the linear deployment of the balloon could have caused changes to the EOM that resulted in this unexpected development. The overall trends of both eccentricity plots match those seen in the binary tests from Figure 4.8.

## 5.2 GPS Case Study

The model was then used to conduct a case study using GPS orbit data to estimate the balloon's impact on this GNSS satellite constellation. The trial used initial values of 26,560 km for the semi-major axis, 0.001 for eccentricity, and 55 degrees for inclination (Teunissen & Montenbruck, 2017). All other initial parameters match those of the best-case solution trials. Figure 5.3 shows how the semi-major axis decreases using these conditions.

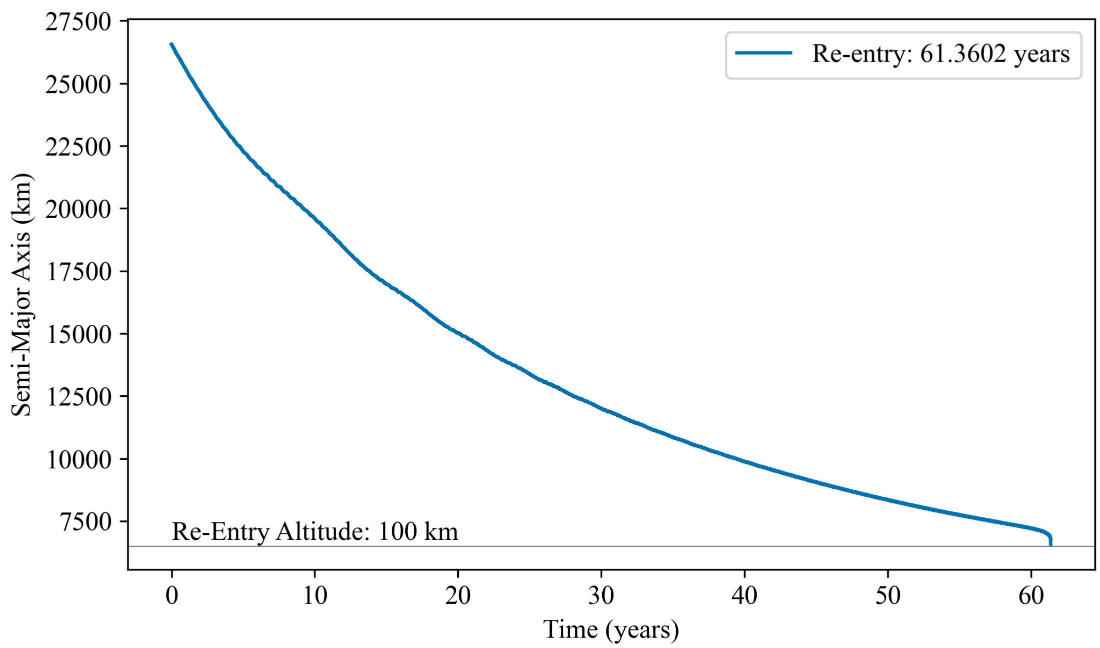


FIGURE 5.3: Semi-major axis in km over time until re-entry for the GPS case study trial using linear inflation and deflation.

As shown in Figure 5.3, when modeling the GPS satellite, re-entry occurs after 61.3602 years. While the initial semi-major axis was 4,560 km larger than all other trials, the trend of this value remained nearly identical. This indicates that the de-orbit process using the spherical solar sail is feasible for orbits with higher altitudes, such as those containing GNSS satellites. The correlating values of the eccentricity over time are displayed in Figure 5.4.

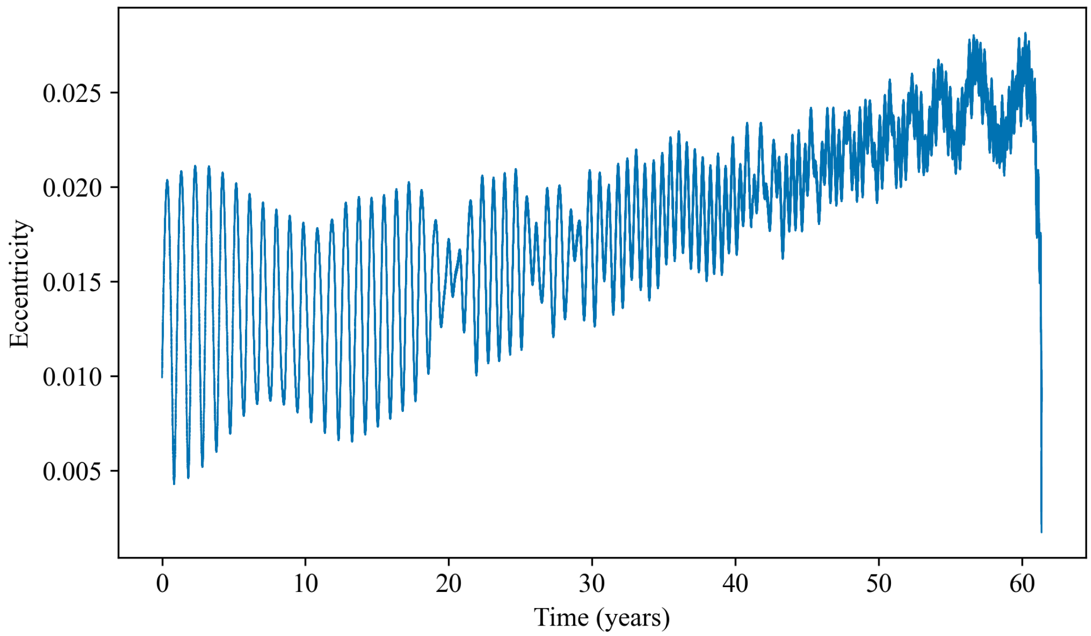


FIGURE 5.4: Eccentricity over time until re-entry for the GPS case study trial using linear inflation and deflation.

While the amplitude of the fluctuating eccentricity values in Figure 5.4 generally decreases over time, the values have a longer periodic increase, matching the trends shown in the 56.06-degree inclination trials, especially later in the process. It should be noted that as the initial eccentricity value was lowered by 0.04, this is likely a factor in the orbital behavior. Furthermore, as the satellite is passing through the 56.06-degree resonance region rather than starting in it, the effects are less uniform, leading to less predictable behavior in the eccentricity.

## 5.3 Spherical Solar Sail Materials

The ideal material for the outer shell of the inflatable balloon must meet several qualifications. First, its optical properties must maximize the perturbations due to SRP by prioritizing reflectivity. Reflected photons will impart more momentum onto surfaces than absorbed photons, thus generating more acceleration. Next, in order to maintain a high area-to-mass ratio, the sail must be as lightweight as possible. The material must also be able to withstand the effects of radiation for very long periods of time. Finally, the balloon must be made of a flexible material with a high enough tensile strength to avoid tearing when the structure is inflated. The material must also be elastic so as to limit permanent deformation during the inflation and deflation processes as much as possible. As mentioned in Chapter 2, the material chosen for the model was a Mylar sheet with an aluminum coating that boasts a reflectivity coefficient of 1.88. Other common materials used for solar sail membranes include Kapton and Teonex, each of which boasts a reflectivity value of 0.9 when coated with 100 nm of Aluminum (Zhao et al., 2023; Kang et al., 2021).

Unfortunately, as these traditional materials are not manufactured to withstand repeated folding and stretching experienced by this balloon, in order for this technology to become applicable to real-life missions, significant improvements in the field of advanced membrane materials must first be made.

## 5.4 Compressor Specifications

In order for the balloon to alter its area-to-mass ratio, there must be a system in place to inflate and deflate it. As a conservative measure, it was decided that the balloon should be able to withstand a maximum pressure difference $P$ of one atmosphere, or approximately 101,325 Pa. Luckily, space is a vacuum, meaning that unlike on Earth, there is no ambient pressure, which reduces the required amount of gas to generate this difference.

Although Helium has traditionally been used to pressurize rigid fuel tanks in space and calculations for its pressure and volume at various temperatures have been conducted (Kwon et al., 2012), it is also used for leak tests due to its small molecular size and quantum tunneling property. Thus, it was decided to use Argon as the inflation gas for the balloon case study, as it can be used for inflatable devices in space.

Given the apparent area-to-mass ratio constraints of 0.04 and 1.0 $m^2/kg$, the cross-sectional area $A_c$ of the fully inflated balloon can be calculated by multiplying these values by the satellite's presumed mass $m_{sc}$ of 100 kg and taking the difference between them:

$$A_c = m_{sc}(AM_{max} - AM_{min}) \tag{5.1}$$

This yields a maximum cross-sectional area of approximately 96.0 $m^2$ for the balloon. Next, the radius of the balloon, $r_b$, can be found using:

$$r_b = \sqrt{\frac{A_c}{\pi}} \tag{5.2}$$

which gives a balloon radius of 5.528 m that can be used to calculate the total volume of the balloon:

$$V_b = \frac{4}{3}\pi r_b^3 \tag{5.3}$$

which comes out to approximately 707.572 $m^3$.

This is an extremely reasonable size for the fully inflated balloon, as NASA's spherical Echo I balloon deployed with a 30.48 m diameter[1], while Echo II boasted an astounding 41 m diameter[2], which is nearly four times the size of the balloon in this study. This number is also promising for real-world applications, as it has been proven possible to construct larger inflatable balloons, which could be used to further improve the re-entry times.

That being said, the inflation of the entire balloon would be extremely inefficient, especially considering that it must be fully inflated and deflated each time the satellite completes an orbit around Earth. As the orbit size decreases, the intensity of the process will rise, with less time to inflate and deflate, and decreased downtime for the compressor. Furthermore, should any space debris puncture a hole in the film, all of the gas inside the balloon would immediately escape, leaving behind another non-functional satellite. Instead, the balloon must have an internal structure stable enough to maintain its spherical shape, yet flexible enough to fold down as much as possible as it deflates.

One option is to line the inner wall of the balloon with closed inflatable film sleeves

[1] NASA Space Science Data Coordinated Archive: Echo I, last accessed: 3 April 2025

[2] NASA Space Science Data Coordinated Archive: Echo II, last accessed: 3 April 2025

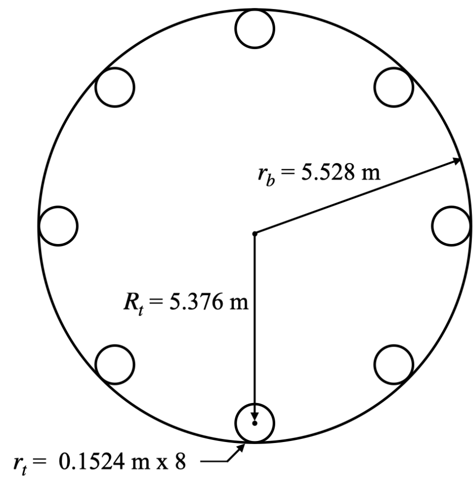


FIGURE 5.5: A section cut of the proposed balloon design. Drawing is not to scale.

that, when filled with gas, would expand the solar sail into its spherical shape. These film sleeves could each be attached to a compressor nozzle at the base of the balloon. For the following calculations, it is assumed that eight equidistantly spaced inflatable film sleeves are used, and that each is perfectly circular with a 0.1524 m (or 6-inch) diameter. A section cut of the proposed balloon design is shown in Figure 5.5.

Each sleeve is assumed to reach from the base of the sphere to its opposite point (the top). While in practice, each sleeve may be sealed off into several different inflatable compartments to prevent the total loss of gas should a collision with debris occur, these calculations assume that each sleeve is a continuous volume. If two sleeves on opposite sides of the balloon are combined and modeled as a single torus inside the sphere with a minor radius $r_t$ of 0.0762 m (or 3 inches), as that is the distance from the shell of the sphere to the centerline of the torus ring, and a major radius $R_t$ found using:

$$R_t = r_b - r_t \tag{5.4}$$

which yields a value of 5.376 m, then the volume of each of the four tori can be calculated as:

$$V_t = 2\pi^2 r_t^2 R_t \tag{5.5}$$

This value can then be multiplied by four (when neglecting to subtract out the intersecting volumes of the four rings) to find that the total volume of the inflated space is approximately 13.623 $m^3$.

According to a survey conducted for the NASA Electronic Parts and Packaging Program, for orbits with altitudes less than 20,000 km, the unmanaged environmental temperatures felt by the spacecraft hardware can range from -65°C to 125°C[3]. As the balloon system has an assumed maximum pressure difference of 1 atm, and the pressure of ideal gases increases at higher temperatures when constrained to a volume, the maximum allowable number of moles of the Argon gas within the system will be calculated using the ideal gas law at a temperature of -65°C, or 208.15 K:

$$PV = n_{mol} R\tau \tag{5.6}$$

where $P$ and $V$ the pressure and volume inside the total ring structure, $n_{mol}$ is the number of moles of Argon, $R$ is the ideal gas constant, and $\tau$ is the absolute temperature. The resulting number of moles of Argon, or 797.801 moles, can be used to find the mass of Argon in the balloon using:

$$m = M_{mol} n_{mol} \tag{5.7}$$

where $M_{mol}$ is the molar mass of Argon. This yields a maximum allowable mass of Argon of 31.871 kg for the balloon inflation system, given the previous assumptions and parameters. Based on the data collected from the best-case solutions in Section 5.1, the minimum semi-major axis experienced by the balloon, $a$, is 6575.53 km from the 56.06-degree trial, which can be used to calculate its minimum period, $T_{min}$, using:

$$T_{min} = 2\pi \sqrt{\frac{a^3}{\mu_\oplus}} \tag{5.8}$$

This equation yields a minimum period of 5306.48 seconds (or about 1.47 hours), which can be used to calculate the maximum mass flow rate, $\dot{m}$, the compressor must be capable of discharging, factoring in the fraction of the period allowed for inflation and deflation,

[3] Environmental Conditions for Space Flight Hardware: A Survey (2005), last accessed: 31 March 2025

$N$, which is set to 32:

$$\dot{m} = \frac{mN}{T_{min}} \tag{5.9}$$

The resulting maximum flow rate that the compressor must be able to discharge is therefore 0.19219 kg/s over 2.764 minutes, considering the outlined circumstances.

Using this same calculation process, the maximum allowable inflation time for GPS satellites and the correlated minimum mass flow rate can be found. By inputting the data from the GPS case study trial, and selecting a temperature of 125°C and semi-major axis of 26,560 km, a minimum mass flow rate of 0.012377 kg/s over about 22.436 minutes was calculated.

To power the compressor, the de-orbiting device could include small solar cells, similar to those employed by Echo I[4], or solar panels, such as those used for Echo II[5]. In either case, each component of the inflatable device is powered by solar energy. Further analysis beyond the scope of this study could be conducted to determine a design for the proposed pump, solar panel placement, and compressed air chamber to fit within the satellite bus.

It should be noted that while current state-of-the-art sleeve designs provide high deployment speeds and small storage volumes, they are less reliable in terms of movement control and are susceptible to plastic deformation when folded (B. Wang et al., 2024). Furthermore, the repeated inflation and deflation may introduce fatigue into the balloon, leading to its eventual failure. While these shortfalls of inflatable devices may be concerning, an investigation into technical solutions is out of the scope of this research.

[4]NASA Space Science Data Coordinated Archive: Echo I, last accessed: 3 April 2025
[5]NASA Space Science Data Coordinated Archive: Echo II, last accessed: 3 April 2025

# Chapter 6

# Summary and Recommendations

## 6.1 Summary

The model was successful in accomplishing the main goals of the study. The results indicate that deploying a spherical solar sail using linear inflation and deflation methods is a feasible de-orbiting method for non-functional GNSS satellites in lower-altitude graveyard orbits and other MEO space debris. When compared with the ideal, binary deployment system, the linear process demonstrated high levels of efficiency. In the best-case solution for a realistic process, this technique is capable of de-orbiting a non-functional GNSS device in a near-circular graveyard orbit with an initial semi-major axis of 22,000 km and an inclination of 56.06 degrees in 50.14 years. For inclinations of 0.001 degrees, the time until re-entry drops to 34.96 years, which is a surprising improvement from the 35.72 years calculated in the binary tests, likely due to the conditions of the satellite's orbit when resonance was encountered. Furthermore, for the GPS case study, re-entry occurred after 61.3602 years.

These times can be cut by increasing the size of the balloon used in the model, as much larger inflatable reflective spheres have been constructed for in-space use before. As perturbations due to atmospheric drag become dominant at altitudes less than 800 km, the analysis window for LEO satellites using this model would be extremely small, but possible. While the proposed de-orbiting technology could also be applicable to retired GEO satellites in graveyard orbits, their high altitudes are not ideal, considering the required computation times. The results of this study are also promising for the prospect of using this technology to send probes back into higher orbits by reversing the timing of the inflation and deflation processes, resulting in a continuous, fuel-less cycle of de-orbiting non-functional satellites.

## 6.2 Recommendations

The proposed technology in this paper is in an exciting phase of development, as there are many complexities that could be introduced to the model. These recommendations cover many aspects of the project and may require their own individual studies should they be pursued.

While the cannonball model is effective for the scope of this research, it presents several restrictions when considering a more realistic model of the satellite:

- First, the entire device is considered to have a single reflectivity coefficient. In reality, it is unlikely that the balloon and the satellite body will be made or coated with the same material, a consideration that could be implemented into future versions of this model.

- Second, the satellite is assumed to have a perfectly spherical shape, regardless of the state of the balloon. Depending on its design, it is possible that the balloon will not maintain a perfectly spherical shape while inflating or deflating. The impact of decreasing symmetry and subsequent generation of SRP torque on the device, as well as the resulting variation in the direction of the resultant force vector, introduces a level of complexity that the current model does not address.

- Further, the shape of the satellite bus attached to the balloon is not currently considered in the model. The impact of the satellite body becoming oriented with the Sun and lowering the apparent area of the balloon for SRP calculations should be considered in future analysis.

Another possible improvement for the model is the optimized prediction of the satellite's trajectory:

- More specifically, the model could be modified to inflate the balloon preemptively while the device is in the Earth's shadow before it begins to travel toward the Sun.

As it stands, the shadow function value bears no impact on the model's decision to inflate or deflate the balloon.

- Furthermore, improvements to the calculation of the trajectory when the satellite is changing direction with respect to the SRP could be made. Currently, the cosine value from Equation 4.1 occasionally flips between positive and negative numbers several times within the integrator when the satellite velocity is nearly perpendicular to the SRP. Each time the sign changes, the inflation or deflation process will begin, which is not an ideal process for an actual pump to experience, though the impact of this discrepancy on the overall results is likely minimal due to the extremely small time steps over which it occurs.

Other aspects of this model that could be developed include the following:

- Future analysis could measure the effects of varying types of inflation and deflation rates, such as exponential inflation, to identify the optimal solution for the deorbiting process.

- Another avenue for future research would be the identification and analysis of the resonances discovered in the long-term binary and best-case solution trials. One current hypothesis is that changing the order and degree of the spherical harmonics coefficients used, and thus, factoring in more than just the $J_2$, could alter the impact of these resonances.

- Finally, the impact of the balloon on satellites in LEOs with atmospheric drag was also out of the scope of this research, but could be of interest in the future, as it will be important to know how the balloon's shape and overall impact on the trajectory will change when the outside air pressure increases.

# Chapter 7

# Model Code Access

All Python software files and descriptions of the program used in the model can be found on the following public GitHub page: https://github.com/tara-eldridge/SRP-Orbital-Simulator.git

# Bibliography

Alessi, E. M., Schettino, G., Rossi, A., & Valsecchi, G. (2017). Solar radiation pressure resonances in low earth orbits. *Monthly Notices of the Royal Astronomical Society*, *473*, 2407–2414. https://doi.org/10.1093/mnras/stx2507

Arshad, M., Bazzocchi, M. C., & Hussain, F. (2025). Emerging strategies in close proximity operations for space debris removal: A review. *Acta Astronautica*, *228*, 996–1022. https://doi.org/10.1016/j.actaastro.2024.12.017

Bryant, R. (1961). The effect of solar radiation pressure on the motion of an artificial satellite. *The Astronomical Journal*, *66*, 430. https://api.semanticscholar.org/CorpusID:121997893

Carvalho, J. P. S., Cardoso dos Santos, J., Lima, J. S., Brejão, L. F., & Prado, A. F. B. A. (2023). A Single-Averaged Model for the Solar Radiation Pressure Applied to Space Debris Mitigation Using a Solar Sail. *Symmetry*, *15*(5), 1107. https://doi.org/10.3390/sym15051107

Curtis, H. D. (2021). *Orbital Mechanics for Engineering Students* (4th ed.). Elsevier. https://doi.org/10.1016/C2020-0-01873-6

Deienno, R., Sanchez, D. M., de Almeida Prado, A. F. B., & Smirnov, G. (2016). Satellite deorbiting via controlled solar radiation pressure. *Celestial Mechanics and Dynamical Astronomy*, *126*(4), 433–459. https://doi.org/10.1007/s10569-016-9699-7

Flury, W. (1991). Collision probability and spacecraft disposition in the geostationary orbit. *Advances in Space Research*, *11*(12), 67–79. https://doi.org/10.1016/0273-1177(91)90544-T

Guerman, A., & Smirnov, G. (2012). Orbital manoeuvres with single-input control. *Advances in the Astronautical Sciences*, *145*, 171–181.

Hairer, E., Norsett, S., & Wanner, G. (1993, January). *Solving Ordinary Differential Equations I* (Vol. 8). Springer Berlin Heidelberg. https://doi.org/10.1007/978-3-540-78862-1

Heaton, A. F., & Artusio-Glimpse, A. (2015). An Update to the NASA Reference Solar Sail Thrust Model. *AIAA SPACE 2015 Conference and Exposition*. https://doi.org/10.2514/6.2015-4506

Hindmarsh, A. C. (1983). ODEPACK, A Systematized Collection of ODE Solvers. *IMACS Transactions on Scientific Computation*, *1*, 55–64. https://computing.llnl.gov/sites/default/files/ODEPACK_pub1_u88007.pdf

Holmes, S., & Featherstone, W. (2002). A unified approach to the clenshaw summation and the recursive computation of very high degree and order normalised associated legendre functions. *J. Geod.*, *76*, 279–299. https://doi.org/10.1007/s00190-002-0216-2

Jacchia, L. (1977, March). *Thermospheric Temperature, Density, and Composition: New Models* (Contract Report No. 375). Smithsonian Astrophysical Observatory. https://ntrs.nasa.gov/api/citations/19770016704/downloads/19770016704.pdf

Jankowitsch, P. (2015, February). The background and history of space law. In F. von der Dunk (Ed.), *Handbook of Space Law*. Edward Elgar Publishing. https://doi.org/10.4337/9781781000366.00010

Johnson, L., Young, R., Barnes, N., Friedman, L., Lappas, V., & McInnes, C. (2012). Solar Sails: Technology And Demonstration Status. *International Journal of Aeronautical and Space Sciences*, *13*(4), 421–427. https://doi.org/10.5139/IJASS.2012.13.4.421

Junshou, C., Wei, T., Chao, L., Guang, Z., & Jie, Y. (2014). History, Present and Future of Solar Radiation Pressure Theory [Series Title: Lecture Notes in Electrical Engineering]. In J. Sun, W. Jiao, H. Wu, & M. Lu (Eds.), *China Satellite Navigation Conference (CSNC) 2014 Proceedings: Volume III* (pp. 41–53, Vol. 305). Springer Berlin Heidelberg. https://doi.org/10.1007/978-3-642-54740-9_4

Kang, J. H., Gordon, K. L., Bryant, R. G., Stohlman, O. R., Wilkie, W. K., Stark, A. E., Barfield, R. S., Sindle, B. R., Finckenor, M. M., & Craven, P. D. (2021). Durability characterization of mechanical interfaces in solar sail membrane structures. *Advances in Space Research*, *67*(9), 2643–2654. https://doi.org/10.1016/j.asr.2020.08.015

Kessler, D. J., & Cour-Palais, B. G. (1978). Collision frequency of artificial satellites: The creation of a debris belt. *Journal of Geophysical Research: Space Physics*, *83*(A6), 2637–2646. https://doi.org/10.1029/JA083iA06p02637

King-Hele, D. (1987). *Satellite orbits in an atmosphere: Theory and applications*. Blackie.

Kozai, Y. (1963). Effects of Solar Radiation Pressure on the Motion of an Artificial Satellite [ADS Bibcode: 1963SCoA....6..109K]. *Smithsonian Contributions to Astrophysics*, *6*, 109. Retrieved March 29, 2025, from https://ui.adsabs.harvard.edu/abs/1963SCoA....6..109K

Krivov, A. V., & Getino, J. (1997). Orbital evolution of high-altitude balloon satellites. [ADS Bibcode: 1997A&A...318..308K]. *Astronomy and Astrophysics*, *318*, 308–314. Retrieved March 31, 2025, from https://ui.adsabs.harvard.edu/abs/1997A&A...318..308K

Krzysztof, S. (2015). Impact of the Atmospheric Drag on Starlette, Stella, Ajisai, and Lares Orbits. *Artificial Satellites*, *50*(1), 1–18. https://doi.org/10.1515/arsa-2015-0001

Kwon, O., Kim, B., Kil, G., Cho, I., & Ko, Y. (2012). Modeling the Prediction of Helium Mass Requirement for Propellant Tank Pressurization. *Journal of Spacecraft and Rockets*, *49*(6), 1150–1158. https://doi.org/10.2514/1.A32073

Lantoine, G., Cox, A., Sweetser, T., Grebow, D., Whiffen, G., Garza, D., Petropoulos, A., Oguri, K., Kangas, J., Kruizinga, G., & Castillo-Rogez, J. (2024). Trajectory & maneuver design of the NEA Scout solar sail mission. *Acta Astronautica*, *225*, 77–98. https://doi.org/10.1016/j.actaastro.2024.08.039

Lappas, V., Adeli, N., Visagie, L., Fernandez, J., Theodorou, T., Steyn, W., & Perren, M. (2011). CubeSail: A low cost CubeSat based solar sail demonstration mission. *Advances in Space Research*, *48*(11), 1890–1901. https://doi.org/10.1016/j.asr.2011.05.033

Mark, C. P., & Kamath, S. (2019). Review of Active Space Debris Removal Methods. *Space Policy*, *47*, 194–206. https://doi.org/10.1016/j.spacepol.2018.12.005

Masalov, A. V. (2019). First Experiments on Measuring Light Pressure I (Pyotr Nikolaevich Lebedev) [Series Title: Springer Series in Optical Sciences]. In R. W. Boyd, S. G. Lukishova, & V. N. Zadkov (Eds.), *Quantum Photonics: Pioneering Advances and Emerging Applications* (pp. 425–453, Vol. 217). Springer International Publishing. https://doi.org/10.1007/978-3-319-98402-5_12

McInnes, C. R. (1999). *Solar Sailing: Technology, Dynamics and Mission Applications* (1st ed). Springer London, Limited.

Montenbruck, O., & Gill, E. (2000). *Satellite Orbits* (1st ed.). Springer Berlin Heidelberg. https://doi.org/10.1007/978-3-642-58351-3

Mori, O., Shirasawa, Y., Mimasu, Y., Tsuda, Y., Sawada, H., Saiki, T., Yamamoto, T., Yonekura, K., Hoshino, H., Kawaguchi, J., & Funase, R. (2014). Overview of IKAROS Mission. In M. Macdonald (Ed.), *Advances in Solar Sailing* (pp. 25–43). Springer Berlin Heidelberg. https://doi.org/10.1007/978-3-642-34907-2_3

Muhleman, D. O., Hudson, R. H., Holdridge, D. B., Carpenter, R. L., & Oslund, K. C. (1960). Observed solar pressure perturbations of echo i. *Science*, *132*(3438), 1487–1487. Retrieved March 29, 2025, from http://www.jstor.org/stable/1707155

Nassiri, N., Mehdizadeh, N., & Jalali, M. (2005). Interplanetary flight using solar sails. *Proceedings of 2nd International Conference on Recent Advances in Space Technologies, 2005. RAST 2005.*, 330–334. https://doi.org/10.1109/RAST.2005.1512586

Office, G. B. N. A., Office, U. S. N. O. N. A., & Office, G. B. H. (2023). *The Astronomical Almanac for the Year 2024: And Its Companion The Astronomical Almanac Online*. U.S. Government Publishing Office. https://books.google.com/books?id=UQdE0AEACAAJ

Petzold, L. (1983). Automatic Selection of Methods for Solving Stiff and Nonstiff Systems of Ordinary Differential Equations. *SIAM Journal on Scientific and Statistical Computing*, *4*(1), 136–148. https://doi.org/10.1137/0904010

Rowe, W. M. (1978). *Sail Materials and Supporting Structure for a Solar Sail, a Preliminary Design, Volume 4* (Contract Report No. 157870). Jet Propulsion Laboratory. Pasadena, CA. https://ntrs.nasa.gov/api/citations/19790007869/downloads/19790007869.pdf

Sanchez, D. M., Yokoyama, T., Brasil, P. I. d. O., & Cordeiro, R. R. (2009). Some Initial Conditions for Disposed Satellites of the Systems GPS and Galileo Constellations (S. M. G. Winter, Ed.). *Mathematical Problems in Engineering*, *2009*(1), 510759. https://doi.org/10.1155/2009/510759

Silva Neto, J. B., Sanchez, D. M., Prado, A. F. B. A., & Smirnov, G. V. (2017). On the Use of Controlled Radiation Pressure to Send a Satellite to a Graveyard Orbit [ADS Bibcode: 2017RMxAA..53..321S]. *Revista Mexicana de Astronomia y Astrofisica*, *53*, 321–332. Retrieved March 30, 2025, from https://ui.adsabs.harvard.edu/abs/2017RMxAA..53..321S

Spaelti, S. B., Liebling, T. M., & Giroux, M. R. (1989). Placement of telecommunication satellites in the geostationary orbit. In D. Pressmar, K. E. Jäger, H. Krallmann, H. Schellhaas, & L. Streitferdt (Eds.), *Operations research proceedings 1988* (pp. 189–194). Springer Berlin Heidelberg.

Spencer, D. A., Betts, B., Bellardo, J. M., Diaz, A., Plante, B., & Mansell, J. R. (2021). The LightSail 2 solar sailing technology demonstration. *Advances in Space Research*, *67*(9), 2878–2889. https://doi.org/10.1016/j.asr.2020.06.029

Teunissen, P. J., & Montenbruck, O. (Eds.). (2017). *Springer Handbook of Global Navigation Satellite Systems*. Springer International Publishing. https://doi.org/10.1007/978-3-319-42928-1

Vallado, D. A., & McClain, W. D. (2007). *Fundamentals of astrodynamics and applications* (3. ed., 1. printing). Microcosm Press [u.a.]

Villela, T., Costa, C. A., Brandão, A. M., Bueno, F. T., & Leonardi, R. (2019). Towards the Thousandth CubeSat: A Statistical Overview. *International Journal of Aerospace Engineering*, *2019*, 1–13. https://doi.org/10.1155/2019/5063145

Vokrouhlicky, D., Farinella, P., & Mignard, F. (1993). Solar radiation pressure perturbations for Earth satellites. 1: A complete theory including penumbra transitions [ADS Bibcode: 1993A&A...280..295V]. *Astronomy and Astrophysics*, *280*, 295–312. Retrieved March 29, 2025, from https://ui.adsabs.harvard.edu/abs/1993A&A...280..295V

Wang, B., Zhu, J., Zhong, S., Liang, W., & Guan, C. (2024). Space deployable mechanics: A review of structures and smart driving. *Materials & Design*, *237*, 112557. https://doi.org/10.1016/j.matdes.2023.112557

Wang, X., Ren, T., Wang, R., Luo, B., Aa, E., Cai, L., Li, M., Miao, J., Liu, S., & Gong, J. (2024). Estimates of Spherical Satellite Drag Coefficients in the Upper Thermosphere During Different Geomagnetic Conditions. *Space Weather*, *22*(11), e2024SW003974. https://doi.org/10.1029/2024SW003974

Zhang, F., Gong, S., Gong, H., & Baoyin, H. (2022). Solar sail attitude control using shape variation of booms. *Chinese Journal of Aeronautics*, *35*(10), 326–336. https://doi.org/10.1016/j.cja.2021.10.036

Zhao, P., Wu, C., & Li, Y. (2023). Design and application of solar sailing: A review on key technologies. *Chinese Journal of Aeronautics*, *36*(5), 125–144. https://doi.org/10.1016/j.cja.2022.11.002